ORTA DOĞU TEKNİK ÜNİVERSİTESİ
FEN BİLİMLERİ ENSTİTÜSÜ MÜDÜRLÜĞÜ

TEZ ŞABLONU ONAY FORMU
THESIS TEMPLATE CONFIRMATION FORM

1. Şablonda verilen yerleşim ve boşluklar değiştirilmemelidir.
2. **Jüri tarihi** Başlık Sayfası, İmza Sayfası, Abstract ve Öz'de ilgili yerlere yazılmalıdır.
3. İmza sayfasında jüri üyelerinin unvanları doğru olarak yazılmalıdır. Tüm imzalar **mavi pilot kalemle** atılmalıdır.
4. **Disiplinlerarası** programlarda görevlendirilen öğretim üyeleri için jüri üyeleri kısmında tam zamanlı olarak çalıştıkları anabilim dalı başkanlığının ismi yazılmalıdır. Örneğin: bir öğretim üyesi Biyoteknoloji programında görev yapıyor ve biyoloji bölümünde tam zamanlı çalışıyorsa, İmza sayfasına biyoloji bölümü yazılmalıdır. İstisnai olarak, disiplinler arası program başkanı ve tez danışmanı için disiplinlerarası program adı yazılmalıdır.
5. Tezin **son sayfasının sayfa** numarası Abstract ve Öz'de ilgili yerlere yazılmalıdır.
6. Bütün chapterlar, referanslar, ekler ve CV sağ sayfada başlamalıdır. Bunun için **kesmeler** kullanılmıştır. **Kesmelerin kayması** fazladan boş sayfaların oluşmasına sebep olabilir. Bu gibi durumlarda paragraf (¶) işaretine tıklayarak kesmeleri görünür hale getirin ve yerlerini **kontrol edin**.
7. Figürler ve tablolar kenar boşluklarına taşmamalıdır.
8. Şablonda yorum olarak eklenen uyarılar dikkatle okunmalı ve uygulanmalıdır.
9. Tez yazdırılmadan önce PDF olarak kaydedilmelidir. Şablonda yorum olarak eklenen uyarılar PDF dokümanında yer almamalıdır.
10. **Bu form aracılığıyla oluşturulan PDF dosyası arkalı-önlü baskı alınarak tek bir spiralli cilt haline getirilmelidir.**
11. Spiralli hale getirilen tez taslağınızdaki ilgili alanları imzalandıktan sonra, [Tez Juri Atama Formu](#) ile birlikte bölüm sekreterliğine teslim edilmelidir.
12. Tez taslaklarının kontrol işlemleri tamamlandığında, bu durum öğrencilere METU uzantılı öğrenci e-posta adresleri aracılığıyla duyurulacaktır.
13. Tez yazım süreci ile ilgili herhangi bir sıkıntı yaşarsanız, [**Sıkça Sorulan Sorular (SSS)**](#) sayfamızı ziyaret ederek yaşadığınız sıkıntıyla ilgili bir çözüm bulabilirsiniz.

1. Do not change the spacing and placement in the template.
2. Write **defense date** to the related places given on Title page, Approval page, Abstract and Öz.
3. Write the titles of the examining committee members correctly on Approval Page. **Blue ink** must be used for all signatures.
4. For faculty members working in **interdisciplinary programs**, the name of the department that they work full-time should be written on the Approval page. For example, if a faculty member staffs in the biotechnology program and works full-time in the biology department, the department of biology should be written on the approval page. Exceptionally, for the interdisciplinary program chair and your thesis supervisor, the interdisciplinary program name should be written.
5. Write **the page number of the last page** in the related places given on Abstract and Öz pages.
6. All chapters, references, appendices and CV must be started on the right page. **Section Breaks** were used for this. **Change in the placement** of section breaks can result in extra blank pages. In such cases, make the section breaks visible by clicking paragraph (¶) mark and **check their position.**
7. All figures and tables must be given inside the page. Nothing must appear in the margins.
8. All the warnings given on the comments section through the thesis template must be read and applied.
9. Save your thesis as pdf and Disable all the comments before taking the printout.
10. **Print two-sided the PDF file that you have created through this form and make a single spiral bound.**
11. Once you have signed the relevant fields in your thesis draft that you spiraled, submit it to the department secretary together with your [Thesis Jury Assignment Form](#).
12. This will be announced to the students via their METU students e-mail addresses when the control of the thesis drafts has been completed.
13. If you have any problems with the thesis writing process, you may visit our [**Frequently Asked Questions (FAQ)**](#) page and find a solution to your problem.

☒ **Yukarıda bulunan tüm maddeleri okudum, anladım ve kabul ediyorum. / I have read, understand and accept all of the items above.**

Name :
Surname :
E-Mail :
Date :
Signature : _____

OPTIMIZATION OF SILICON-OXYNITRIDE THIN FILMS FOR
CRYSTALLINE SILICON (C-Si) PERC CELL

A THESIS SUBMITTED TO
THE GRADUATE SCHOOL OF NATURAL AND APPLIED SCIENCES
OF
MIDDLE EAST TECHNICAL UNIVERSITY

BY

HASAN HÜSEYİN CANAR

IN PARTIAL FULFILLMENT OF THE REQUIREMENTS
FOR
THE DEGREE OF MASTER OF SCIENCE
IN
PHYSICS

JUNE 2022

Approval of the thesis:

OPTIMIZATION OF SILICON-OXYNITRIDE THIN FILMS FOR CRYSTALLINE SILICON (C-Si) PERC CELL

submitted by **HASAN HÜSEYİN CANAR** in partial fulfillment of the requirements for the degree of **Master of Science** in **Physics, Middle East Technical University** by,

Prof. Dr. Halil Kalıpçılar
Dean, Graduate School of **Natural and Applied Sciences**   _____

Prof. Dr. Seçkin Kürkcüoğlu
Head of the Department, **Physics**   _____

Prof. Dr. Raşit Turan
Supervisor, **Physics, METU**   _____

Prof. Dr. Ayşe Çiğdem Erçelebi
Co-Supervisor, **Physics, METU**   _____

Examining Committee Members:

Prof. Dr. Uğur Serincan
Physics, Eskişehir Technical University   _____

Prof. Dr. Raşit Turan
Physics, METU   _____

Assoc. Prof. Dr. Selçuk Yerci
Electrical and Electronics Eng., METU   _____

Assoc. Prof. Dr. Emre Yüce
Physics, METU   _____

Prof. Dr. Gülnur Aygün Özyüzer
Physics, Izmir Institute of Technology   _____

Date: 20.06.2022

I hereby declare that all information in this document has been obtained and presented in accordance with academic rules and ethical conduct. I also declare that, as required by these rules and conduct, I have fully cited and referenced all material and results that are not original to this work.

Name Last name : Hasan Hüseyin Canar

Signature :

ABSTRACT

OPTIMIZATION OF SILICON-OXYNITRIDE THIN FILMS FOR CRYSTALLINE SILICON (C-Si) PERC CELL

Canar, Hasan Hüseyin
Master of Science, Physics
Supervisor : Prof. Dr. Raşit Turan
Co-Supervisor: Prof. Dr. Ayşe Çiğdem Erçelebi

June 2022, 63

PECVD deposited SiN_x has been used in PV industry especially for PERC solar cell as anti-reflection coating (ARC) and passivating layer [1]. However, its limited optical and electrical properties create a barrier for achieving higher solar cell efficiencies. For that reason, an alternative is introduced that is SiO_xN_y thin film with adjustable refractive index can be tuned as low as SiO_2 [2].

In this thesis, deposited SiN_x and SiO_xN_y films were characterized by various measurement methods such as SE, FTIR, C-V and PCD. FTIR measurements revealed that H content of the films increases for higher refractive indices. While Q_f of the SiN_x films becomes higher, D_{it} reduces significantly for lower indices. SiO_xN_y film with index of 1.73 has the smallest D_{it} value which is related to higher Si-O density. Fabricated symmetrical samples showed that depositing few nm of SiO_xN_y layer beneath the SiN_x film improves iV_{oc} values of both n and p-type undoped wafers.

Q_f of Al_2O_3/SiN_x stack with lower index of SiN_x film improved with peak firing temperature. iV_{oc} values resisted to higher peaks which is attributed to lower H content in the SiN_x film.

Optimized ARC layers were simulated with OPAL 2 for comparing absorption/reflection losses [3]. SiN_x with lower index at the interface reduced the absorption of light in the thin film. Also, depositing SiO_xN_y on top of SiN_x film resulted in lower reflection in U-V region compared to single layer SiN_x film. In the scope of the simulation results, J_{Gen} improved with absolute 0.19 mA.cm^{-2}.

According to I-V results of the fabricated PERC solar cells, J_{sc} values were in the same trend as the simulation results, thus resulting in higher photoconversion efficiency.

Keywords: PECVD, silicon nitride, silicon oxynitride, passivation, PERC

ÖZ

SİLİSYUM OKSİNİTRÜR İNCE FİLMLERİN KRİSTAL SİLİSYUM (C-Si) PERC TİPİ HÜCRE İÇİN OPTİMİZASYONU

Canar, Hasan Hüseyin
Yüksek Lisans, Fizik
Tez Yöneticisi: Prof. Dr. Raşit Turan
Ortak Tez Yöneticisi: Prof. Dr. Ayşe Çiğdem Erçelebi

Haziran 2022, 63

PECVD ile biriktirilen SiN_x ince filmi özellikle PERC güneş hücre tipinde yansıma önleyici ve pasivasyon tabakası olarak PV endüstrisinde yaygın olarak kullanılmaktadır [1]. Fakat optik ve elektriksel özelliklerinin kısıtlı olması yüksek güneş hücresi verimlerine ulaşılmasına engel olmaktadır. Bu sebeple alternatif olarak optik sabiti silisyum dioksit (SiO_2) tabakası değerlerine inebilen SiO_xN_y ince filmi geliştirildi [2].

Bu tezde, biriktirilen SiN_x ve SiO_xN_y filmleri SE, FTIR, C-V ve PCD gibi çeşitli ölçüm metotlarıyla karakterize edildi. FTIR ölçümleri, filmlerin optik sabiti arttıkça H miktarlarının arttığını ortaya koydu. SiN_x filminin optik sabiti azaldıkça Q_f değeri daha yüksek değerlere ulaşırken D_{it} değeri önemli ölçüde azaldı. Si-O yoğunluğunun daha yüksek olmasından dolayı en düşük D_{it} değeri optik sabiti 1.73 olan SiO_xN_y filmi ile elde edildi. Üretilen simetrik örnekler, SiN_x filminin altına birkaç nanometre SiO_xN_y katmanının biriktirilmesisin hem n hem de p-tipi katkısız gofretlerin iV_{oc} değerlerini geliştirdiğini gösterdi.

Tepe ısıl işlem sıcaklığı artışı ile Al_2O_3/SiN_x yığınının daha düşük optik sabitli SiN_x filminin Q_f değeri gelişti. iV_{oc} değerlerinin daha yüksek tepe sıcaklıklarına direnmesi, SiN_x filmindeki düşük H miktarı ile ilişkilendirildi.

Yansıma/sönümleme kayıplarını karşılaştırmak için optimize edilen ARC tabakaları, OPAL 2 ile simüle edildi [3]. Ara yüzeye biriktirilen düşük optik sabitli SiN_x filmi ile ışığın ince film içerisinde sönümlenmesi azaldı. Ayrıca tek başına biriktirilen SiN_x katmanına kıyasla, SiN_x üzerine SiO_xN_y filminin biriktirilmesi U-V bölgesinde yansımanın azalmasıyla sonuçlandı. Simülasyon sonuçları kapsamında, J_{Gen} değeri net 0.19 $mA.cm^{-2}$ olarak gelişti.

Üretilen PERC güneş hücrelerinin I-V sonuçlarına göre, J_{sc} değerleri simülasyon sonuçlarıyla aynı eğilimde olduğu görüldü ve böylelikle daha yüksek fotodönüşüm verimleri elde edildi.

Anahtar Kelimeler: PECVD, silisyum nitrür, silisyum oksinitrür, pasivasyon, PERC

To my family

ACKNOWLEDGEMENTS

TABLE OF CONTENTS

LIST OF TABLES

LIST OF FIGURES

FIGURES

xvi

LIST OF ABBREVIATIONS

ABBREVIATIONS

PERC :   Passivated Emitter and Rear Contact

Al_2O_3 :   Aluminium oxide

ALD :   Atomic layer deposition

PECVD :   Plasma Enhanced Chemical Vapor Deposition

SiN_x :   Silicon Nitride

SiO_xN_y :   Silicon Oxynitride

H :   Hydrogen

Si :   Silicon

PV :   Photovoltaics

FTIR :   Fourier Transform Infrared Spectroscopy

SE :   Spectroscopic ellipsometer

D_{it} :   Interface state density

Q_f :   Fixed charge density

PCD :   Photoconductance decay

C-V :   Capacitance-Voltage

G-V :   Conductance-Voltage

iV_{oc} :   implied open-circuit voltage

J_{Gen} :   Generated current density

LIST OF SYMBOLS

SYMBOLS

$E_{F,M}$: *metal and p-Si fermi level*

$\Phi_{M,P}$: *p-Si work function*

Φ_P : *semiconductor work function*

E_c : *conduction band*

E_v : *valence band*

E_i : *intrinsic energy level*

Φ_s : *surface potential*

N_a : *bulk doping concentration*

n_i : *intrinsic carrier concentration*

T : *temperature in Kelvin*

q : *elementary charge*

V_G : *gate voltage*

C_i : *insulator capacitance*

C_d : *depletion capacitance*

ϵ_i : *insulator dielectric constant*

ϵ_0 : *permittivity of free space (8.85 E-14 F.cm^{-1})*

ω : *wavenumber [cm^{-1}]*

$\Delta\Phi_{MS}$: *metal-semiconductor work function difference*

σ :   *conductivity*

ϵ_{si} :   *dielectric constant of Si 11.8 ϵ_0*

p_0 :   *bulk doping concentration*

CHAPTER 1

INTRODUCTION

Fossil fuel had entered the life of mankind in the late 18th ' s. With the industrial revolution, factories started using coal for compensating energy demand. Then, coal was integrated into transportation system because water vapor used in steam turbines was not enough for generating enough power for long rides. In 1848, James Young discovered petroleum was a turning point in the industry. The use of petroleum in industry ramped up the mass production. Also, generating electricity with burning petroleum had become widespread. For all these astounding contribution of fossil fuels in history, the Earth had faced with greenhouse gases which plays active role in global warming. In the middle of the 20th century, scientists tried to find alternative sources for generating electricity. Proposal of the photo electric effect [4] by Albert Einstein in 1905 gave birth to the production of one of the most popular renewable energy device known as solar cell by Bell Laboratories (1954). The basic idea under working principle of solar cell was converting light coming from the Sun to generate electricity. It was an important invention that it is a nature friendly power generator and offers unlimited power.

Continuing research and development in the science brought about improvements in the solar cell industry. Nowadays, there are plenty of solar cell models contributed to the literature such as PERT, PERC, IBC and TopCON. One of the most known, simplest and widely used model is PERC.

1.1   PERC Solar Cell

Standard PERC solar cell shown in *Figure 1.1* is made up of a diode with a p-n junction model. n+ region is made by doping 5A group element of Phosphorus to Si bulk that will create a depletion region with a strong electric field. When light enters the diode, electron and hole pairs will be formed. By forming a potential difference, charged particles can be collected in an external circuit to generate electricity. Surface of the Si is highly recombinative and results in reduction in collected current. To avoid this issue, surface is covered with dielectric materials such as SiN_x, SiO_xN_y and Al_2O_3 that passivates recombination centers. Surface of the cell that directed toward the Sun has a textured surface which helps the device to reduce surface reflection and allowing more light to enter the Si for generating higher current, thus more power. For collection of charged particles, ohmic contact should be satisfied. Aluminium and Silver metal contacts are screen-printed to both rear and front surfaces respectively.
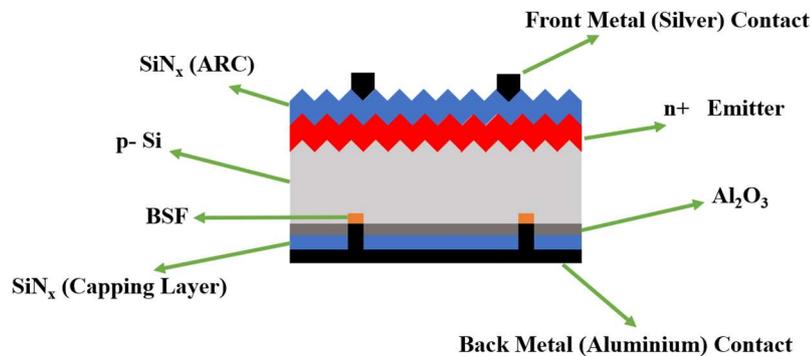
Figure 1.1. PERC solar cell.

1.2   PECVD Deposited SiN_x and SiO_xN_y Films

SiN_x and SiO_xN_y thin films are amorphous materials that are widely used in microelectronics and PV industry due to their tunable optical and electrical properties. They are deposited by PECVD system with help of plasma. The precursor gas sources are SiH_4 (Silane), NH_3 (Ammonia) and N_2O (Nitrous oxide). They can be used to reduce surface reflection and passivating the defect centers. While the refractive index of the SiN_x film varies between 1.8 and 3, SiO_xN_y film has wider index range with 1.5 to 3.0. With contributing wide range of optical band-gap, they do reduce the reflection to increase J_{Gen} in the Si. Moreover, the deposition process brings positive Q_f [5] that satisfies external electric field to repel minority carriers away from the surface. Also, incorporated H atoms release during the fast-firing step and reduces surface and Si-bulk defect centers [6]. They do protect the another used passivation layer known as Al_2O_3 that has negative Q_f [7]. While SiN_x/SiO_xN_y films repel positive charges from the front surface, Al_2O_3 with its negative Q_f repels negative charges from the rear surface for reducing recombination at the Si surface. With the SiN_x/SiO_xN_y films on the front surface, p-n junction in Si and Al_2O_3 film on the rear surface, the band diagram of the solar cell is illustrated as in the following *Figure 1.2*.
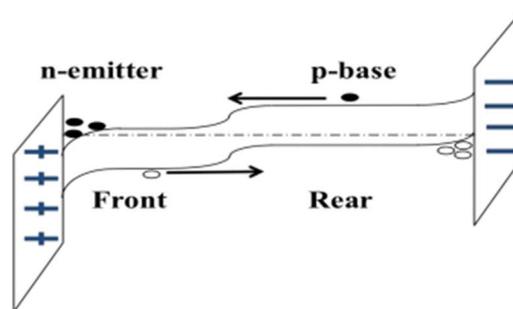
Figure 1.2. Band diagram of PERC solar cell with presence of Q_f[8].

CHAPTER 2

THEORY AND BACKGROUND

PECVD deposited SiN_x improves surface recombination by passivating D_{it} over Si-SiN_x interface with H diffusion during fast firing process [9]. Also, positive Q_f comes with non-stoichiometry, repels minority carriers by supplied electric field. Hence, passivation of Si is improved in terms of chemically and electrically.

2.1   Chemical Passivation

Over the Si-SiN_x interface there are bunch of D_{it} (*Figure 2.1*) which act as recombination center. These states can be passivated by H during the fast-firing step. In the literature, D_{it} values for the SiN_x deposited interfaces vary between 1.1E10 to 8.6E11 $cm^2.eV^{-1}$ [1]. For higher index of SiN_x, H content reaches to maximum value; however, D_{it} increases with the Si content. After firing process, lifetime values increase for lowering D_{it} [10].
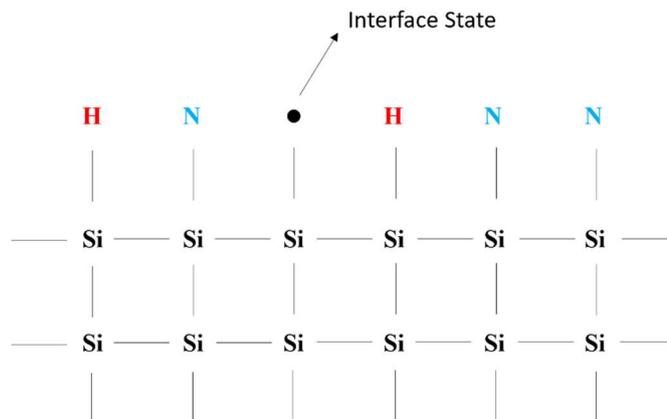
Figure 2.1. Illustration of interface state density at Si-SiN_x interface.

2.1.1 IR Spectrum of SiN$_x$

SiN$_x$ is an IR active dielectric film. Its main components are Si-H, N-H and Si-N bonds where these bonds mostly belong to stretching vibrational mode. IR spectrum of SiN$_x$ can be seen in the *Figure 2.2*.
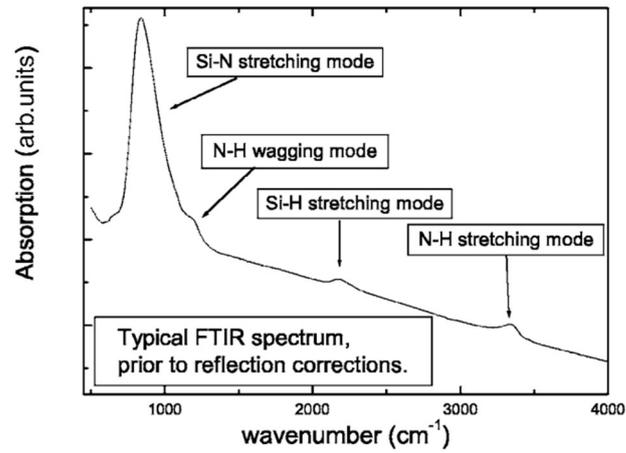
Figure 2.2. IR absorption spectrum of silicon nitride in 400-4000 cm^{-1} [11].

Locations and calibration factors of the SiN$_x$/SiO$_x$N$_y$ IR modes for specific molecules given in the literature [12]–[15] are collected in the following Table 2.1.

Table 2.1. *Position, mode and calibration factors (K) of Si-N, Si-H and N-H bonds.*

Si-N		
Position (cm^{-1})	**Mode**	**K (cm^{-2})**
790	Si-N	2E19
850	N-Si$_3$	2E19
950	H-SiN$_3$	2E19

Si-H		
Position (cm^{-1})	**Mode**	**K (cm^{-2})**
2000	H-Si-Si$_3$	7E19
2060	H-Si-HSi$_2$	11E19
2100	H-Si-NSi$_2$	17E19
2140	H-Si-SiN$_2$/H-Si-HSiN	11E19
2170	H-Si-HN$_2$	40E19
2220	H-Si-N$_3$	20E19

N-H		
Position (cm^{-1})	**Mode**	**K (cm^{-2})**
3240	?	?
3340	N-H	12E19
3450	NH$_2$	50E19

Calibration factor/Absorption cross-section (K) values are calculated by determination of density of films with help of Nitrogen ion bombardment. It has an importance in quantitatively determination of H concentration of SiN$_x$ films [16].

2.1.2 Hydrogen Content of SiN$_x$ Films

2.1.2.1 Lanford and Rand Method

Hydrogen has an important role in cell structure as passivating defects and hence, it enables lower surface recombination rates. In 1978, Lanford and Rand found a method which helps one to determine H content inside the SiN$_x$ films [17]. To do this, they extracted absorption cross-sections/calibration factors (K) for Si-H and N-H stretching modes. Although they found only for 2175 and 3340 cm^{-1} peaks, followers found that there were many of them as shown in Table 2.1.

As proposed by Aydınlı et al. [18], one must convert absorbance into absorption coefficient by using the following eq. (2.1),

$$\alpha = 2.303 \frac{A}{d}$$
Eq. (2.1)

where A is absorbance (a.u.) and d is thickness of the film in (cm)

Then, deconvoluting interested peaks and done baseline correction, area under each peak is integrated.

$$[X - H] = K \int \frac{\alpha(\omega)}{\omega} d\omega = K \, \alpha_{max}$$
Eq. (2.2)

According to the position of peaks, related calibration factor (K) is multiplied by the result, the maximum absorption coefficient, as shown in the eq. (2.2).

2.2   Electrical Passivation

As described in MIS section that positive Q_f of SiN_x creates accumulation layer which keeps minority carriers away from the surface.
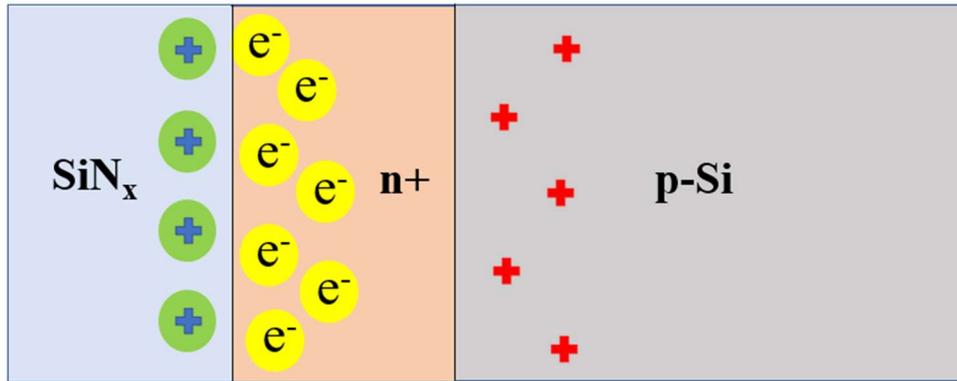
Figure 2.3. Accumulation of electrons on the front surface due to Q_f.

In *Figure 2.3*, minority carriers (holes) are forced to move towards bulk and recombination of carriers decreases. In this way, electrical passivation of the silicon is provided.

2.2.1   Positive Q_f of SiN_x Films

During the deposition of SiN_x, Si atom bonds with three N atoms to make $N_3 \equiv Si \cdot$ and leaves one unpaired electron. This structure is known as K-center and referred as dangling bond [19]. Those defects are randomly distributed in the SiN_x film. Regions close to the Si-bulk, unpaired electron is donated to the Si and leaves behind K^+ (eq. 2.3) which acts as positive charge and they can be found up to 20 nm away from the Si-SiN_x interface [20].

$$K^0 \rightarrow K^+ + e^- \qquad\qquad \text{Eq. (2.3)}$$

The Q_f varies between 10^{11} - 5.10^{12} C/cm^2 and it depends on stoichiometry of the film [21], [22]. SiN_x with higher refractive index has lower Q_f than films with lower refractive indices. Optimum Q_f is required for best surface passivation of solar cells. N-type substrates are perfectly passivated by SiN_x due to polarity of charges which repel minority carriers (positive) and reduce surface recombination [23].

2.2.2 MIS (Metal-Insulator Semiconductor) Capacitor

MIS structure is crucial for obtaining interface properties, crucial for passivation of c-Si, of thin films. One can get information about Q_f and D_{it} of the deposited films top of c-Si.
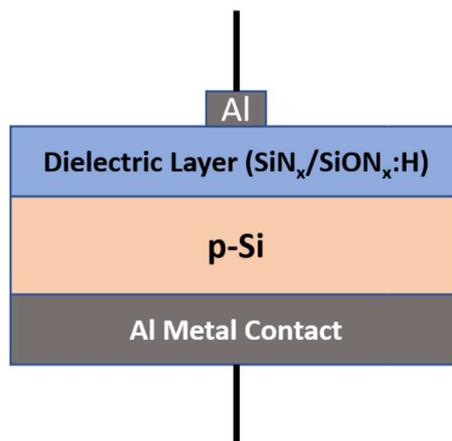
Figure 2.4. Structure of the MIS capacitor.

In an ideal case, it is expected to be that there will not be any charge contribution from dielectric layer and no interface states. However, due to unbounded bonds which are called as "K-centers" act as positive charges. Hence, this fact results in bending of valence and conductance bands. To obtain information about Si-SiN_x interface, it is required to fabricate a MIS capacitor, capable of responding applied bias voltage with varying frequency. As it can be seen from the *Figure 2.4* that

dielectric layer deposited on a c-Si in between metal contacts will result in a capacitor.
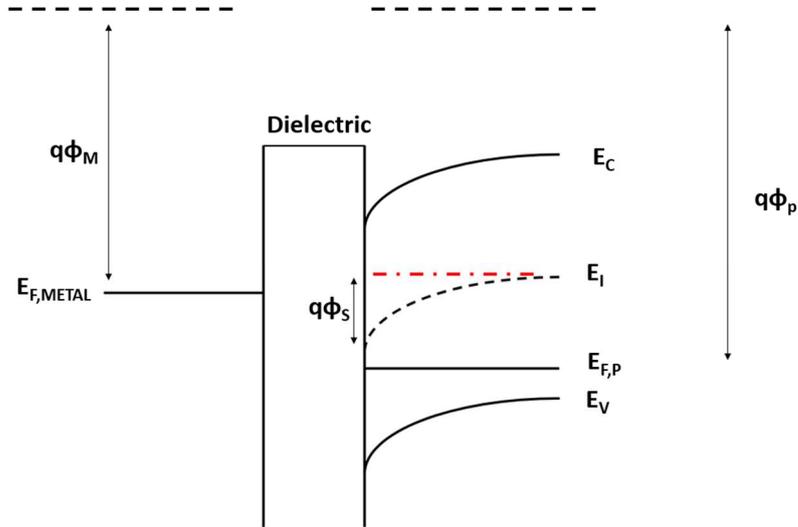
Figure 2.5. Illustration of energy levels of MIS capacitor.

In *Figure 2.5*, the energy levels of metal and p-Si are given when a dielectric layer stacked between them. When positive voltage applied to metal side, net potential of the electrons will be reduced, and semiconductor energy levels will be bent to compensate that potential difference. The potential difference formed due to energy level bending on the semiconductor side is called as surface potential. It shows the strength of the bending.

$$V_g = V_i + \Phi_S \qquad \text{Eq. (2.4)}$$

Since SiN_x/SiO_xN_y has Q_f, electrons move closer to the interface and creating an inversion layer where electron concentration is higher than bulk doping. Inversion value can reach to at most $2\Phi_F$ in eV. This value is calculated by the given formula,

$$q\Phi_S = 2q\Phi_{F,P} = 2kTln\left(\frac{N_a}{n_i}\right) \qquad \text{Eq. (2.5)}$$

where k is Boltzmann constant and kT value is taken as 0.0259 eV

In an ideal MIS capacitor, it is assumed that there is no Q_f and D_{it} to occur at the dielectric/semiconductor interface. As it can be seen from the *Figure 2.5*, applied voltage bends the semiconductor energy levels. Here, fermi levels remain the same because no current passes through dielectric [24].

When negative voltage applied, holes from the bulk start to accumulate to the surface will create accumulation layer. Altering the polarity of the applied voltage, these electrons will be pulled to the interface and will remain positive ions behind. At the surface, inversion layer will occur, and it is depleted, and so-called space charge region will occur. Since holes respond quickly, accumulation capacitance will be higher. However, electrons in the inversion layer are created by thermal generation, they are signal dependent and for high frequency values, inversion layer capacitance remains lower. The total capacitance of such a system can be shown as,

$$C_{Total} = \frac{C_i C_d}{C_i + C_d} \qquad \text{Eq. (2.6)}$$

In accumulation, C_{Total} *is just* C_i because no accumulation occurs but in inversion, series combination of C_i and C_d dominates together. Hence, total capacitance stays lower than accumulation. Since minority carriers respond to applied voltage, for low frequency values inversion layer capacitance reaches to accumulation capacitance value. Also, it can be satisfied by illuminating the device so that carrier generation will increase the total capacitance.
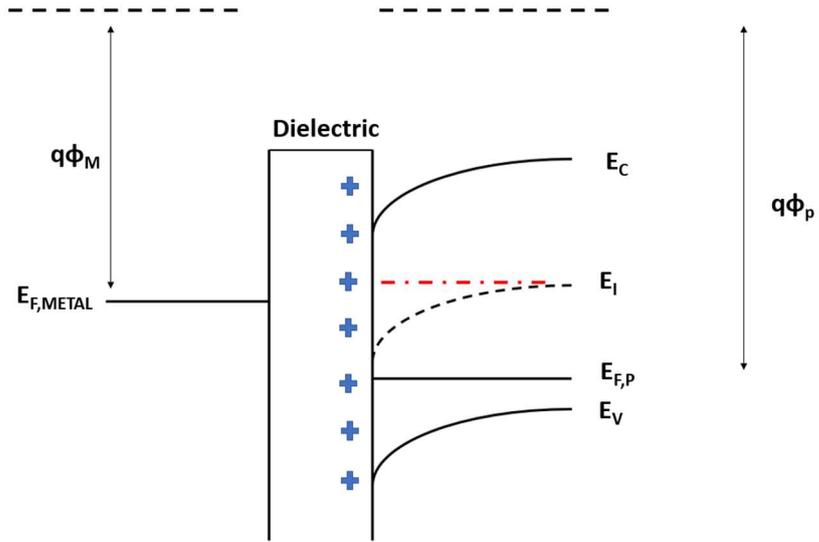
Figure 2.6. Dielectric layer with positive Q_f.

It is inevitable to have dielectric without Q_f and D_{it}. Generally, in PV field commonly used dielectrics are amorphous SiN_x, SiO_xN_y and Al_2O_3. SiN_x/SiO_xN_y have positive Q_f and Al_2O_3 layer has negative Q_f. SiN_x/SiO_xN_y bend the Si energy levels without applying voltage and create inversion layer by inducing negative charges in the semiconductor. Although V_{FB} is just equal to the applied voltage, those induced charges will also be accounted in calculation of flat-band. New equality holds as,

$$V_{FB} = \Delta\Phi_{M,S} - \frac{Q_f}{C_i} \qquad \text{Eq. (2.7)}$$

D_{it} acts as trap centers for minority carriers and increases surface recombination. D_{it} contributes to the depletion capacitance by filling states below fermi level.
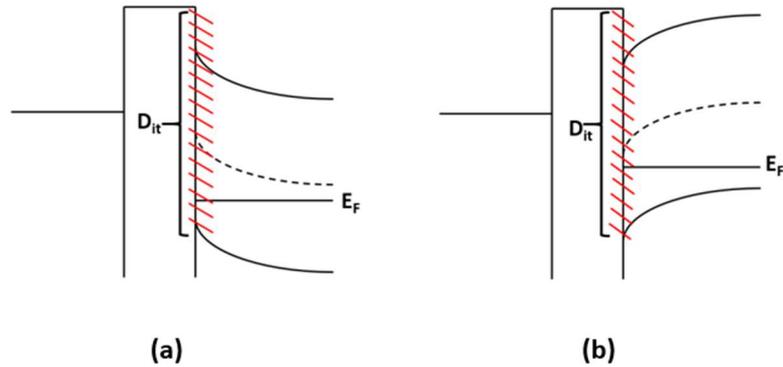
Figure 2.7. D_{it} distribution along the c-Si and SiN$_x$ interface during accumulation (a) and inversion (b) conditions.

D_{it} is distributed over the interface. D_{it} can be filled by swiping applied voltage. p-Si is used as an illustration which can be seen in *Figure 2.7*. When negative voltage is applied, bands will bend upward near the interface (accumulation condition) (*Figure 2.7* (a)) and below the fermi level, all states are assumed to be filled by electrons. In the case of inversion condition, bending will be toward downward (*Figure 2.7* (b)).
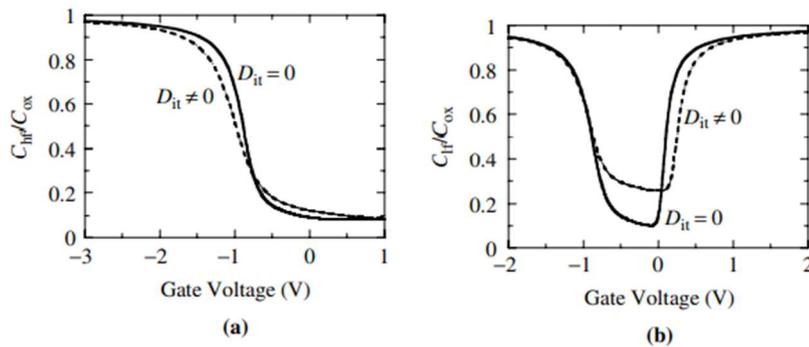
Figure 2.8. Stretch-out along the voltage axes in the absence of C_{it} (a) and capacitance curve in the presence of C_{it} (b) [25].

D_{it} does respond to the applied frequency. Since minority carriers do not follow the high frequency signal, C_{it} becomes 0 and C_{dep} dominates. On the contrary, at low frequency condition (*Figure 2.8* (b)), carriers will follow the signal but this time capacitance around the depletion will move upward. This is mainly because of D_{it}. Also, at high frequency measurements (*Figure 2.8* (a)), capacitance curve stretches-out along the voltage axis where total capacitance does not change.

2.2.3   Conductance

Swapping of energy levels around fermi level will change the conductivity of the fabricated capacitor. When traps release carriers, conductivity is increased, and this can be measured by conducting C-V measurements.

$$G = \frac{1}{R} = \frac{\sigma\ A}{d} \hspace{5cm} \text{Eq. (2.8)}$$

Conductance is inverse of resistance and its formulation is shown by eq. (2.8). In a regular measurement, equivalent circuit looks like Figure 2.9(a) where C_m and G_m stands for measured values. However, realistic case is much more complicated and represented by *Figure 2.9* (b). Unavoidably, measured conductance and capacitance require correction due to possible experimental or device caused series resistance. They could be metal contact-probe, bulk impurities, Si-metal contact caused problems.
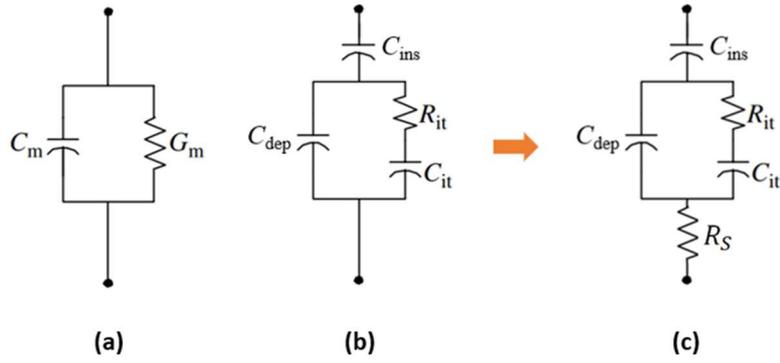
Figure 2.9. Equivalent circuit models for MIS-Capacitor. Simplified model which is what it is measured (a) and model which shows the realistic case (b). Corrected circuit with additional R$_s$ (c).

Following equations can be used to eliminate series resistance problem [26]

$$R_S = \frac{G_a}{G_a^2 + (\omega C_a)^2}$$ Eq. (2.9)

$$a = G_m - [G_m^2 + (\omega C_m)^2]R_s$$ Eq. (2.10)

$$C_C = \frac{[G_m^2 + (\omega C_m)^2]C_m}{a^2 + (\omega C_m)^2}$$ Eq. (2.11)

$$G_C = \frac{[G_m^2 + (\omega C_m)^2]a}{a^2 + (\omega C_m)^2}$$ Eq. (2.12)

where C$_a$ and G$_a$ are the values measured in accumulation region.

2.2.4   Measurable Constants from MIS Capacitor

Capacitance-voltage measurement is so effective that we can get valuable properties of bulk, interface between dielectric/silicon bulk and dielectric. We can list them as follow,

- Insulator capacitance
- Bulk Doping Concentration
- Flat-Band Voltage
- Fixed Charge Density of Insulator
- Surface Potential
- Interface State Density over c-Si interface

2.2.4.1   Insulator Capacitance

Capacitance of a MIS-capacitor can easily be obtained by taking the accumulation layer capacitance value at high-frequency (1 MHz) where it is saturated.

2.2.4.2   Bulk Doping Concentration

One can find the bulk doping concentration by taking the inverse square of the capacitance-voltage graph. By using the inverse square C-V graph, slope of the depletion layer [27] can be used to calculate doping concentration of by

$$N_A = \frac{2}{q\epsilon_{Si}} \frac{1}{slope\ A^2}$$

Eq. (2.13)

where A represents metal contact area in cm^2

2.2.4.3　Flat-Band Voltage

In the presence of fixed charges, we can obtain flat-band voltage easily by using inverse square graph of capacitance [28]. Extrapolation of the depletion part on x-axis is just the flat-band voltage itself.

2.2.4.4　Fixed-Charge Density

In an ideal MOS-capacitor, no bend bending occurs but dielectric films bring inevitable charge density due to disruption of c-Si and dielectric material at the interface. Hence, stable bending occurs together with the density of these charges. We can use the following equation to calculate Q_f,

$$Q_f = (\Delta\Phi_{M,S} - V_{FB})\frac{C_i}{qA} \qquad\qquad \text{Eq. (2.14)}$$

2.2.4.5　Surface Potential

Energy levels bend due to existence of Q_f and change in applied voltage. The bending is shown by surface potential, and it is useful in calculating D_{it} distribution over c-Si. Surface potential can be calculated by using the following Berglund integral [29],

$$V_s = q \int_{Vfb}^{V}\left(1 - \frac{C_{LF}(V)}{C_i}\right)dV \qquad\qquad \text{Eq. (2.15)}$$

The above-mentioned eq. (2.15) gives the surface potential over applied gate voltage. Also, D_{it} distribution over Si-band gap energy level can be found by using the calculated V_s values together with Si wafer dopant concentration. The following equation is used to find the energy level of Si with respect to the surface potential [30].

$$E = V_S + \frac{kT}{q} \ln\left(\frac{p_0}{n_i}\right) \qquad\qquad \text{Eq. (2.16)}$$

2.2.4.6 Interface State Density

- **Conductance Method**

Measured conductance of the device parallel to the capacitance shows the release and de-trap of carriers by the interface states. D_{it} can be calculated over the c-Si by measuring conductance while scanning from low to high frequency. Then, applying appropriate series resistance correction to the measured conductance using the eq. (2.12) and plotting conductance with respect to the frequency, one can get the following *Figure 2.10*,
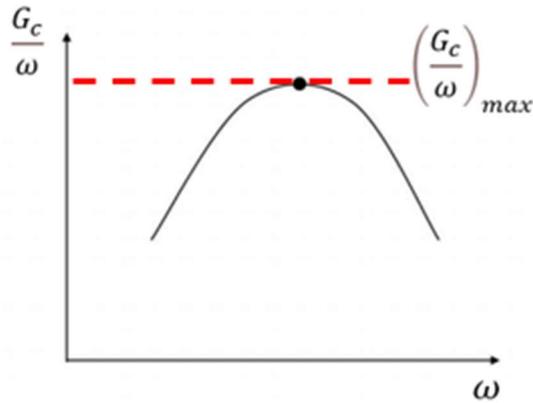
Figure 2.10. Conductance vs. frequency graph. Max. value is used to calculate D_{it}.

Maximum value read from the curve is inserted into the eq. (2.17) to get D_{it}.

$$D_{it} \sim \frac{2.5}{qA} \left(\frac{G_C}{\omega}\right)_{max} \qquad\qquad \text{Eq. (2.17)}$$

CHAPTER 3

EXPERIMENTAL

3.1   Sample Preparation

3.1.1   Specifications of Wafers

In the complete study, industrial 156.75 x 156.75 mm^2 size; p type wafers were used.

Table 3.1. *Specifications of wafers used in the experiment.*

Specifications	
Brand	LONGi
Dopant	Boron
Orientation	1 0 0
Thickness (µm)	180±20
Base Resistivity	0.95±0.10

3.1.2   Surface Modification via Chemical Process

Manufacturers slice silicon ingots with help of wire to get wafers to be used in industry. These wafers are called as as-cut and process cause surface damage which is bad for passivation. Also, the surface of these wafers is not eligible for ARC purposes. In that manner, some chemicals are used to shape the surface. Alkaline chemical (KOH) is used to remove the damaged surface by reducing the thickness of the wafers. This process is called SDE (saw damage etching).
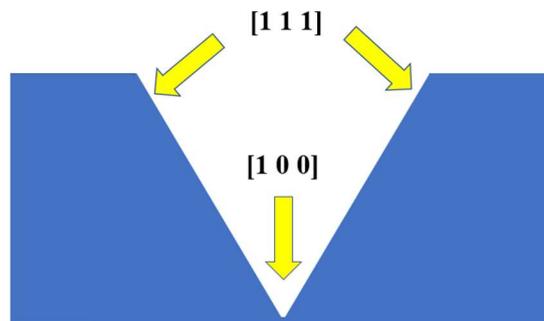
Figure 3.1. Lattice structure of Si surface after KOH processing.

Further continuing this process leads to change in surface orientation of c-Si. KOH solution etches silicon surface with different rates. Etch rate is highest in downward direction but rate starts to decrease on the sides. It is seen in the *Figure 3.1* that sides have lattice structure of [1 1 1] and in downward [1 0 0]. In the end, 2-3 µm in height pyramidal structures are formed on the surface. This process is mainly called as texturing.

Wafers are laid on a cylindrical rolling carrier and required chemicals are already filled inside the zones just underneath the cylinder. While wafers are moving, in the first zone HF reacts with PSG and removes it. Then, top of the textured wafer is covered by water not to damage pyramids; however, pyramids on the bottom of the wafers are removed by using HF, H_2SO_4, HNO_3 and DI-water. Hence, single side etching (SSE) process is completed.

3.1.3   Emitter Formation (POCl$_3$ Diffusion)

Emitter is a need for diode formation. POCl$_3$ gas is used for n+ emitter formation by diffusion. PSG layer is formed on both surface of the wafers in furnace under atmospheric conditions where N_2 and O_2 are used as precursors. Then, Phosphorus atoms inside the PSG layer are driven inside the Si at high temperatures. Width of

the emitter region is around 0.3-0.5 µm. Measured sheet resistance of the regions was 87 Ω/sq.

3.1.4 Al_2O_3 Deposition

TMA and di-Water vapor is used for Al_2O_3 deposition. Device is set to 200°C and wafers are inserted horizontally to the trace. With help of N_2, wafer moves back and forth around the reactor zone. It is so fast that it repeats this cycle around 50 times in a minute. During each cycle 0.13 nm alumina layer is deposited. Optimum thickness of 5 nm of Al_2O_3 was deposited on etched surface of the wafers. Post annealing followed the deposition at 425°C for 15 min. in an annealing furnace for stabilization of Al_2O_3 layer.

3.1.5 SiN_x and SiO_xN_y Deposition

SiN_x/SiO_xN_y as capping and ARC layers were deposited by DG-Plasma direct PECVD system at low frequency. Films were deposited at 170 Pa and 450°C with varying process gases; SiH_4, NH_3, N_2 and N_2O. Variation in the gas flows results in change in stoichiometry of the film.

3.1.6 LCO (Laser Contact Opening)

Locally ablation of the dielectric layers at the rear surface was held by a picosecond laser works at 532 nm of wavelength.

3.1.7 Screen Printing

For the metallization process, 5 busbar-129 finger printing mask was used at the front surface with silver paste, where Aluminium paste was used at the rear surface. Fast

firing process was done at conveyor belt for the formation of Al-BSF. The metal fraction of the front surface is 5.83 %. The total area of the cells were 244.3 cm^2.

3.1.8 Samples for SE and FTIR Measurement

As-cut wafers with given specifications in Table 3.1 were underwent SDE process and surface cleaning was done to remove native oxide layer. Then, samples were loaded into PECVD system for SiN_x and SiO_xN_y deposition. Samples were cut into 3 x 3 cm^2 small pieces with help of a laser marker for SE and FTIR measurements.

3.1.9 Samples for C-V Measurement

Surface cleaning procedure followed the SDE process. For the case of samples with 5 nm of Al_2O_3/SiN_x stack layers, first 5 nm of Al_2O_3 was deposited and activated before SiN_x deposition. Then, samples with and w/out 5nm of Al_2O_3 layer were loaded into PECVD system for SiN_x deposition. Selected samples were fired in a conveyor belt for Hydrogenation process. Samples were cut into 3 x 3 cm^2 small pieces. 150 nm of Al was evaporated with an E-Beam system under vacuum. While uncoated side of the samples were fully covered with Al, front surface of the samples was covered with hard mask made from Si wafer had small openings for contact formation with a diameter of 600 μm. The front contact area of the samples was 2.83 E-3 cm^2. MIS capacitors were annealed at 350°C for 30 min. to have good metal contact [31]. Finally, devices measured with HP Impedance Analyzer with varying bias voltage with swapping frequencies from 8 kHz up to 3 MHz.

3.1.10 Samples for PCD (Photoconductance Decay) Measurement

To test front surface dielectric performance, emitter formation was done on textured wafers in a diffusion furnace with $POCl_3$ gas. The sheet resistance of the emitter was

87 Ω/sq. Afterwards, PSG layer was removed by surface cleaning procedure and ARC layers were deposited with PECVD system.

To test rear surface passivation performance, textured wafers were double side etched and then, 5 nm of Al_2O_3 layer were deposited symmetrically on both surfaces with ALD system. Symmetrically deposition of 120 nm of SiN_x capping layer on both surfaces followed the activation of Al_2O_3 layer.

All samples were cut into 9 equal pieces and various firing temperatures were tested. iV_{oc} values were measured for both non-fired and fired samples by WCT-120TS lifetime tester device produced by Sinton Instruments [32].

3.1.11   Samples for I-V and EQE Measurements

Textured wafers were dipped into HF/HCl solution for removing native oxide layer. Then, emitter with sheet resistance of 87 Ω/sq were formed in a phosphorus diffusion furnace. One side of the wafers were etched and 5 nm of Al_2O_3/SiN_x capping layer were deposited. ARC layer was deposited after depositing rear surface passivation layers. After completing LCO and screen-printing steps, PERC solar cells were fired in a conveyor belt. Finally, calibrated AAA class flash simulator device was used to test performance of fabricated solar cells.

3.2   Experimental Plan

3.2.1   Characterization of SiN_x and SiO_xN_y Films

As shown in *Figure 3.2*, three groups of samples were prepared to observe relation between film stoichiometry and its characteristics (optical, chemical, electrical). Stoichiometry of the films were changed by varying process gas flows.
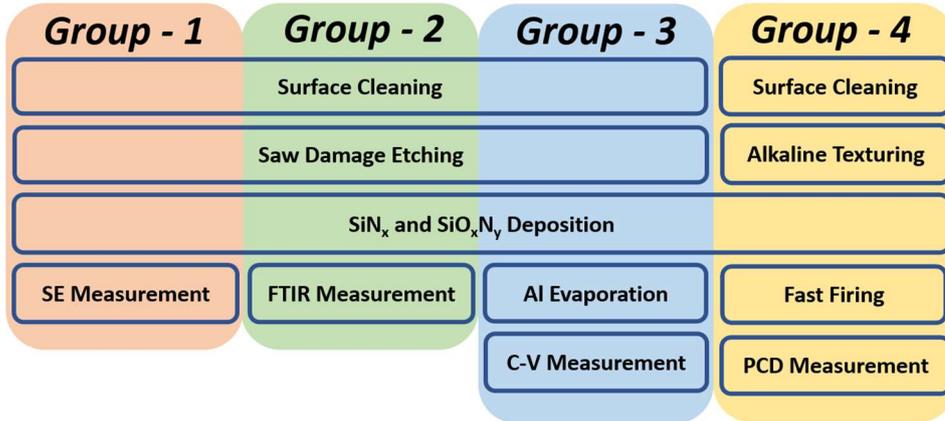
Figure 3.2. The sample preparation flow for characterizing fabricated films.

3.2.2 Rear Surface Passivation: Optimization of Capping SiN$_x$ Deposited on 5 nm of Al$_2$O$_3$ Layer

An extensive experimental plan shown in *Figure 3.3* was conducted to optimize capping SiN$_x$ layer on 5 nm of Al$_2$O$_3$ layer. In this plan four groups of samples were fabricated to investigate H degradation mechanism on Si-bulk, influence of SiN$_x$ stoichiometry on fixed charge density of Al$_2$O$_3$ layer, passivation stability in terms of iV$_{oc}$ with various peak firing temperatures and solar cell performance of Al$_2$O$_3$/SiN$_x$ stacks.
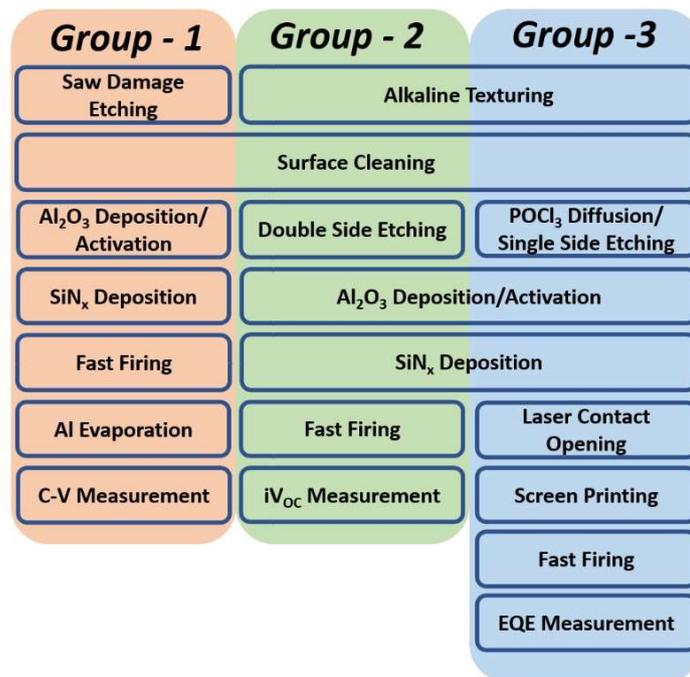
Figure 3.3. The sample preparation flow for investigating SiN_x stoichiometry on passivation quality of Al_2O_3/SiN_x stacks.

3.2.3   Front Surface Passivation: Optimization of ARC Layer

In this step, after determining best Al_2O_3/SiN_x stack layer on rear surface passivation, ARC layer was studied extensively by fabricating symmetrical samples, C-V analysis, cell performance and reflection simulation. For the reflection simulations, obtained optical constants from SE measurements were uploaded into OPAL2 which simulates SiN_x/SiO_xN_y stack layers with user inputs [3]. Symmetrical samples and fabricated PERC solar cells had n+ emitter regions with a sheet resistance of 87 Ω/sq.
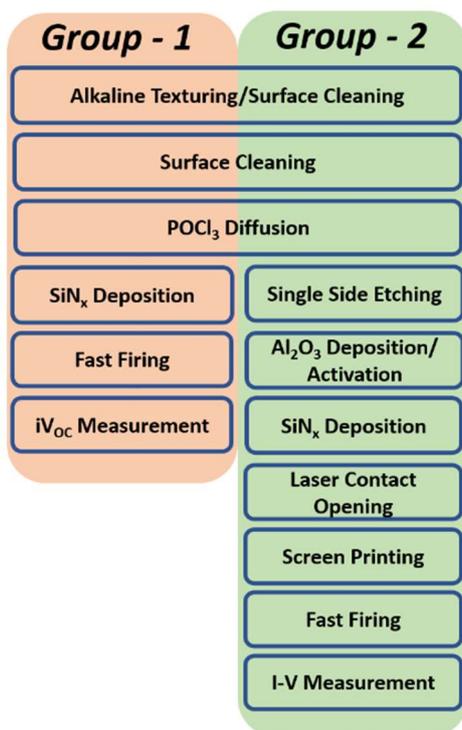
Figure 3.4. The sample preparation flow for observing passivation and cell performance of optimized ARC layers.

CHAPTER 4

RESULTS AND DISCUSSION

4.1 Characterization of SiN$_x$ and SiO$_x$N$_y$ Films

Fabricated samples with different surface morphologies were analyzed to obtain valuable properties of films such as optical constants, interface properties and H density.

4.1.1 Optical Constants

Stoichiometry of the SiN$_x$ and SiO$_x$N$_y$ layers were changed by variying sent process gas flows. Deposited films on SDE wafers were cut into 3 x 3 cm^2 pieces for SE measurement. Optical constants like film thickness, refractive index, extinction coefficient and optical band-gap of each film were measured with using Cauchy with Urbach Tails and Tauch-Lorentz fit models. For modeling the samples, c-Si/SiN$_x$/Surface Roughness/Air combination is used as suggested by Jellison et al [33]. Measured extinction coefficients (k) for the thin films were converted to absorption coefficient (α) by using the following formula,

$$\alpha = \frac{4\pi k}{\lambda}$$
Eq. (4.1)

In Table 4.1, sent gas flows during the deposition process of each recipe are given with corresponding measured refractive index values.

Table 4.1. *Gas flows of the deposited films with corresponding refractive indices (n) at 632 nm of wavelength.*

Film	Gas Flows / n	SiH$_4$ (sscm)	NH$_3$ (sscm)	N$_2$O (sscm)	N$_2$ (sscm)
SiO$_x$N$_y$	1.60	300	1200	4600	2000
	1.73	400	800	2400	2000
SiN$_x$	1.96	314	5186	0	0
	2.04	611	4889	0	0
	2.18	900	4600	0	0
	2.31	1070	4430	0	0
	2.53	1375	4125	0	0
	2.98	2025	3475	0	0

It is obvious from Table 4.1 that increasing SiH$_4$ flow results in higher refractive index for the SiN$_x$ films.
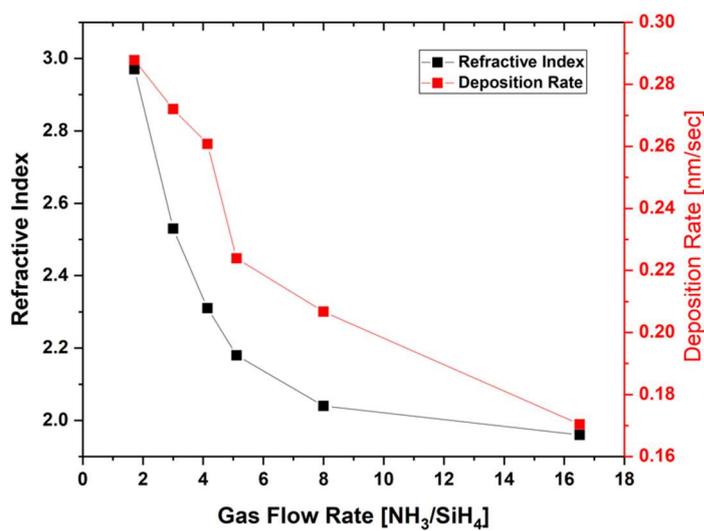
Figure 4.1. Variation of refractive index and deposition rate of SiN$_x$ films for different gas flow rates.

In *Figure 4.1*, change in deposition rate and refractive index of the films are given with respect to variation in gas flow rates. Reduction in gas flow rate results in higher deposition rate. Other words, SiH_4 is driving the deposition rate of the reaction. Wan et al. also reported that reduction in gas flow rate results in higher refractive index values [34].
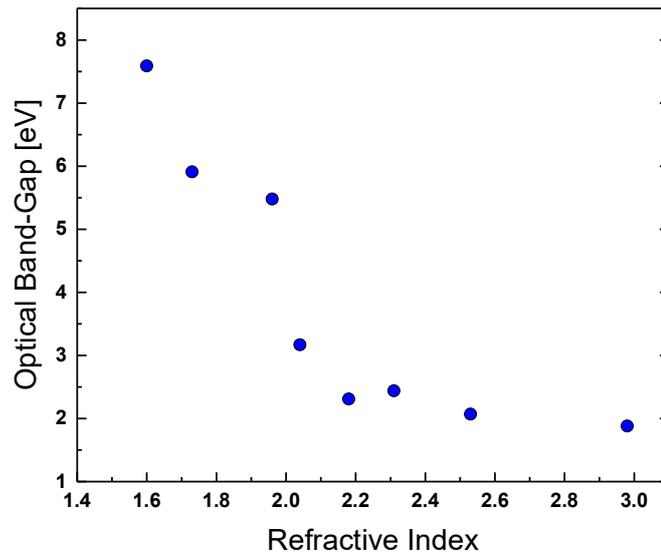
Figure 4.2. Optical band-gap of the fabricated SiN_x and SiO_xN_y films.

Figure 4.2 shows the variation of optical band-gap values of the fabricated films with changing refractive index. Optical band-gap of SiO_xN_y reaches to almost 8 eV that is nearly the band gap of SiO_2 [35]. Optical band-gap of SiN_x with refractive index of 1.96 reaches to 6 eV while SiN_x film with refractive index of 2.97 can be as low as 2 eV. Use of SiO_xN_y films allows one having wider optical window. Obtained optical band-gap values for the higher indices are in well aggrement with [36],[33]. While Grigaitis et al. reported the band-gap value for lower index of SiN_x as high as 5.14 [37] which is quite closer to the result shown in *Figure 4.2*, elsewhere showed that it remained as low as 3.8 eV for the same refractive index [36].
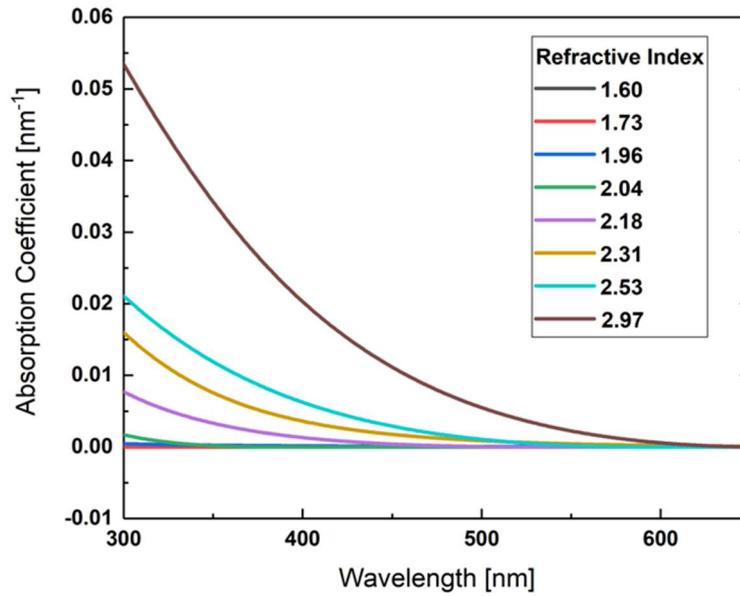
Figure 4.3. Absorption coefficient curves of the fabricated SiN$_x$ and SiO$_x$N$_y$ films in the wavelength range of 300-650 nm.

Figure 4.3 shows the measured absorption coefficient curves of the fabricated SiN$_x$ and SiO$_x$N$_y$ films. Absorption of light in the 300-600 nm of wavelength region is increasing with higher refractive index due to higher Si concentration in SiN$_x$ layer. SiO$_x$N$_y$ films with refractive index of 1.60 and 1.73 has no absorption in the given region. Moreover, SiN$_x$ with 1.96 has almost no absorption while 2.04 has considerably lower absorption.

4.1.2   IR Spectrum and H Density
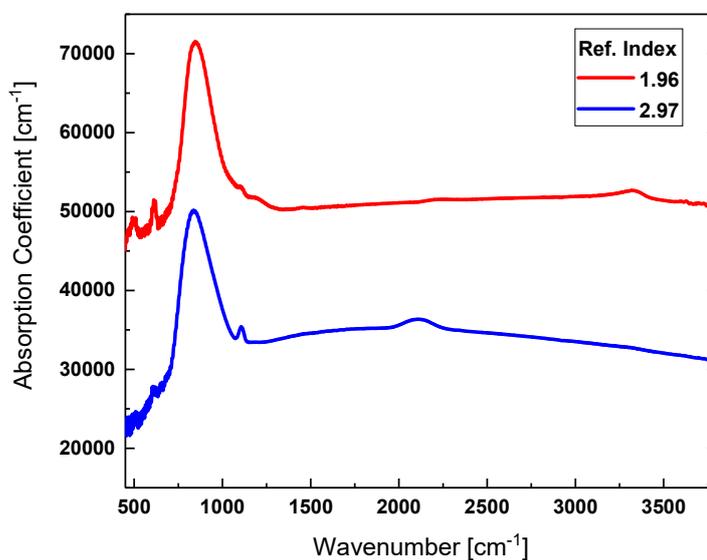
Figure 4.4. IR spectrum of the fabricated SiN_x films with refractive index of 1.96 (red) and 2.97 (blue) in the wavenumber range of 450-3800 cm^{-1}.

Figure 4.4 shows the IR spectrum of two SiN_x films with refractive indices 1.96 and 2.97. Si-N, Si-H and N-H stretching modes of the films are available in the range of 700-1000 cm^{-1}, 2000-2300 cm^{-1} and 3300-3400 cm^{-1} respectively. While SiN_x film with index of 2.97 has strong Si-H peak centered around 2100 cm^{-1}, the other has a strong N-H peak centered around 3300 cm^{-1}. It is mainly due to lack of Si atoms in the stoichiometry of SiN_x film.
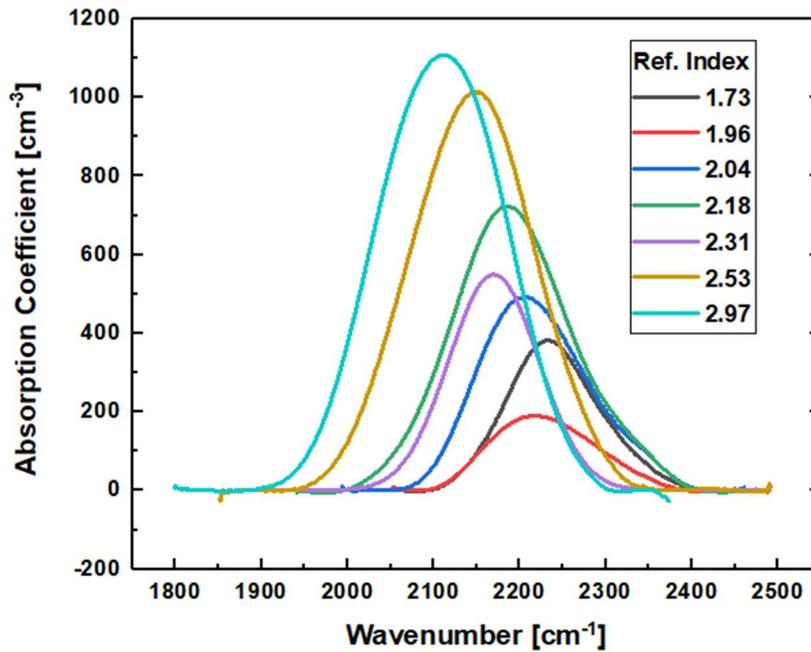
Figure 4.5. Si-H stretching peaks of the fabricated SiN_x and SiO_xN_y films.

In *Figure 4.5*, Si-H stretching peaks of the fabricated films with various stoichiometries are shown. By lowering the refractive index of the films, Si-H peak position of the films tend to move toward higher wavenumbers [38]. According to the given molecular structures of each Si-H mode in Table 2.1, H atoms bond with Si atoms which are bond with N atoms in the case of lower refractive indices. In addition, SiO_xN_y with refractive index of 1.60 has no trace of Si-H peak or it is at the noise level.

The deconvolution of the Si-H stretching mode is done similar to one found in the study published by Hanyaloğlu (1998) [39]. Calculated absorption coefficients of the relative deconvoluted peaks are given in the Table 4.2. The shift of Si-H peaks toward lower wavenumber with increasing refractive index is clear from the α value of each individual peak. Moreover, absorption coefficients of N-H peaks are increasing with lowering the refractive index for the SiN_x films. There is no peak found centered around 3450 cm^{-1} for N-H stretching mode; however, peak centered at 3240 cm^{-1} is

34

available for all films except SiN_x with index of 2.97. Since there is no calibration factor found in the literature for the peak centered at 3240 cm^{-1}, same factor is used for it. There is no trend observed for the SiO_xN_y films for the N-H mode.

Table 4.2. *Obtained absorption coefficients of Si-H and N-H stretching modes after deconvoluting for each stoichiometry.*

	Wavenumber [cm^{-1}]				
n	**Si-H Stretching**			**N-H Stretching**	
	2090	*2170*	*2240*	*3240*	*3350*
1.60	-	-	-	261.41	261.08
1.73	-	-	378.92	190.29	288.68
1.96	-	105.31	137.76	292.43	673.98
2.04	-	293.49	375.24	91.33	326.38
2.18	67.25	585.16	257.36	83.06	194.94
2.31	132.57	549.18	217.33	46.44	122.38
2.53	261.28	719.06	79.35	79.15	133.99
2.97	977.20	380.00	-	-	-

Contrary to the SiN_x films, SiO_xN_y films have Si-O bond centered around 1040 cm^{-1} [40], [41] as a result of sent N_2O gas during the process. Comparison of deconvoluted Si-O symmetrical stretching mode for fabricated two SiO_xN_y films are shown in *Figure 4.6*. Although N_2O gas flow for the film with index of 1.60 is higher than 1.73 one, Si-O density is lower for film with index of 1.60. This is mainly because of lower SiH_4 gas flow sent during the deposition of the film and O atoms could not be able to find excessive Si atoms to bond with.
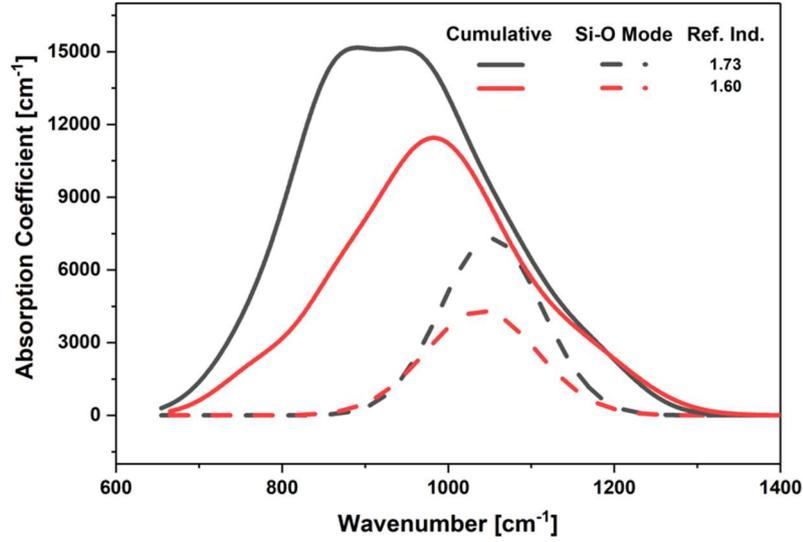
Figure 4.6. Deconvoluted Si-O symmetric stretching modes (centered at 1040 cm^{-1}) at from the cumulative peaks in the 650-1400 cm^{-1} wavenumber region of the SiO$_x$N$_y$ films.

In *Figure 4.7*, calculated H density of the fabricated films are given by using eq. (2.1). H density increases for higher refractive indices. Although this result is well correlated with Bredemeier et. al 2019 [42], the order of magnitude is one order higher; however, Boulesba et al. reported the calculated H density in the same other with what we have found [40]. Since H atoms bond with molecules that have plenty of Si atoms or N atom incorporated molecules which are poor in the films with higher refractive indices.
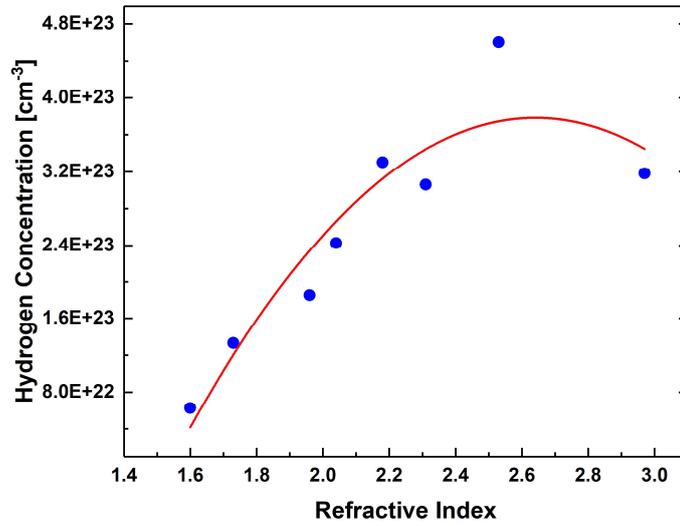
Figure 4.7. Calculated H density of fabricated SiN_x and SiO_xN_y films.

4.1.3 C-V Measurements and Interface Properties

Interface properties of the SiN_x and SiO_xN_y films were studied by fabricated MIS devices that fabrication process flow was given in section 3.1.9. An image of the contact area with a diameter of 600 μm taken from optical microscope is shown in *Figure 4.8*.
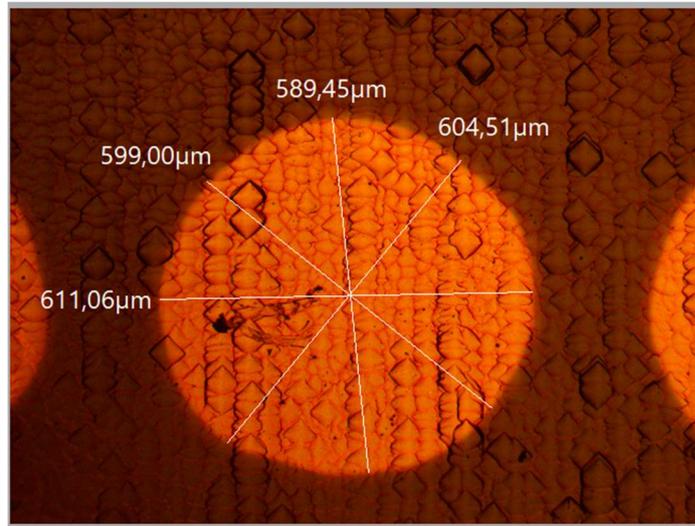
Figure 4.8. Optical microscope image of the contact region of the fabricated MIS device with a diameter of 600 µm.

Every measurement was taken by sweeping applied bias voltage from negative to positive values. Insulator capacitance value measured at 1 MHz of frequency while fixed charge densities of each film were calculated by using that capacitance value where it was in accumulation. Eq. (2.14) was used for the calculation of fixed charge density. Φ_m value was taken from the literature as 4.23 eV [43]. After completing measurements, all data sets were corrected by the series resistance correction as shown in the section 2.2.3.

Measurements were taken at frequencies between 8 kHz to 3 MHz to calculate interface state density. An example of regular low-frequency C-V measurement result taken at 10 kHz on the sample with index of 2.53 is shown in *Figure 4.9*. It is obvious from the C-V graph that the device responds to low-frequency signal at inversion. The peak around the depletion region on the conductance graph results from the carriers captured by interface traps and used for calculation of D_{it}.
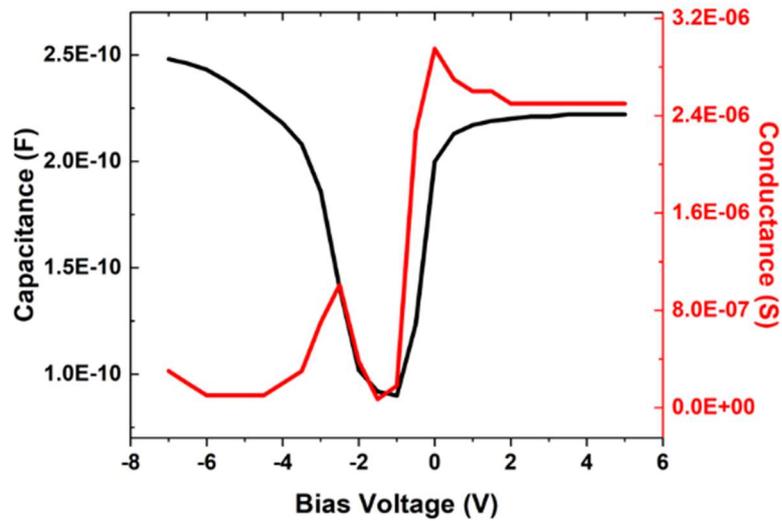
Figure 4.9. Measured C-V and G-V graph of the dielectric layer with index of 2.53 sample measured at low (10 kHz) frequency.

Measured C-V and G-V graphs of SiN$_x$ film with index of 2.53 at high frequency measurement (1 MHz) is shown in the *Figure 4.10*. Since the thermally generated carriers do not follow the high frequency signal, capacitance in inversion region remains lower. Moreover, comparing the conductance graphs in *Figure 4.9* and *Figure 4.10*, a sharp increase in inversion region is related to the capacitance effect in the inversion [44].
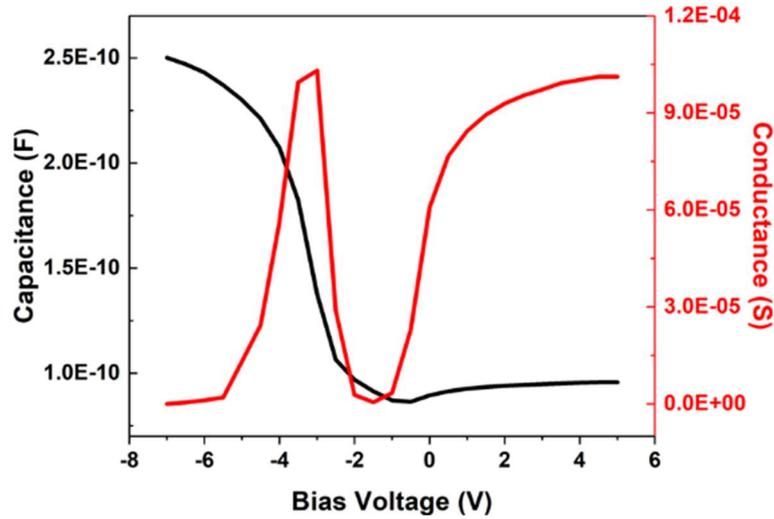
Figure 4.10. Measured C-V and G-V graph of the dielectric layer with index of 2.53 sample measured at high (1 MHz) frequency.

For the calculation of interface state density, conductance method which was proposed by Nicollian is used [45]. The method is based on the variation of conductance around the depletion region due to change in the response of traps at each frequency [46]. Then, the maxima of the peak on the G/ω vs freq. plot was used to calculate D_{it} by eq. (2.17). Conductance peaks over frequency for the fabricated films are shown in *Figure 4.11*. The stated curves are representing the mid-gap conductance variation of the trap states. The energy distribution of the states was determined by calculating surface potential with help of Berglund Integral given in section 2.2.4.5.
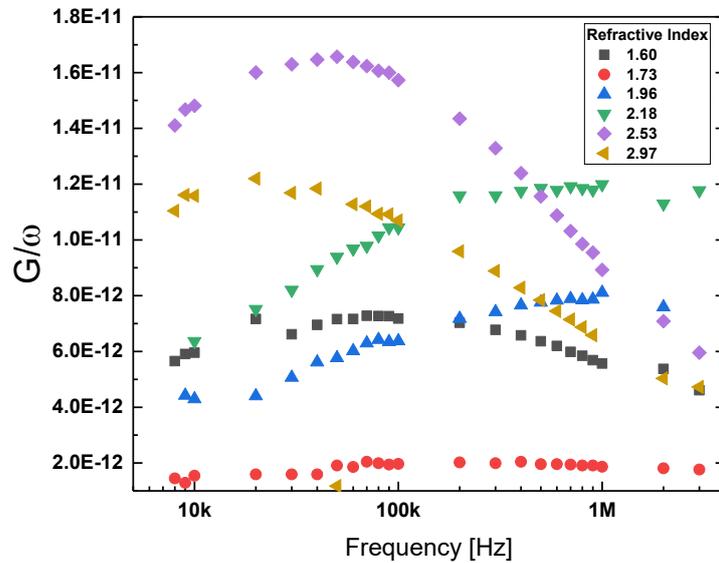
Figure 4.11. G/ω vs freq. curves for the films with different index at mid-gap.

Figure 4.12 shows the variation of Q_f and D_{it} values over stoichiometry of the films. Q_f of SiN_x films are reducing exponentially as going from lower to higher refractive indices [22]. Q_f of SiN_x films are increasing with lowering refractive index that is well correlated with the Lelievre (2009) and Sharma (2013) [22], [8]. The increase is attributed to the enlargement in the number of back-bonding structures of N atoms with Si ($N_3 \equiv Si \cdot$). Contrary to what Lelievre et al. (2009) claimed on variation of D_{it} of the SiN_x films, D_{it} is reducing for lower refractive indices that is in a good agreement with Basa et al. (2000) [47] . According to their study, the root of the D_{it} is silicon dangling bonds due to excessive Si atoms in SiN_x stoichiometry. In the case of less Si content in the film, those dangling bonds are diminished by excessive N atoms [48]. Although no trend observed for the SiO_xN_y films, lowest D_{it} value is obtained from SiO_xN_y film with index of 1.73. SiN_x with index of 2.97 has slightly lower D_{it} value from 2.53 that is attributed to the release of H atoms during the deposition process at 450°C and chemical passivation reduced the D_{it} values over

interface [22]. Comparing the deconvoluted Si-O mode of the SiO_xN_y films in *Figure 4.6*, film with index of 1.73 has higher Si-O density than 1.60. Lower D_{it} is attributed to the higher Si-O density that is in a good agreement with the literature [49],[50]. As a remark, MIS capacitor from SiN_x films with refractive indices of 2.04 and 2.31 were not fabricated.
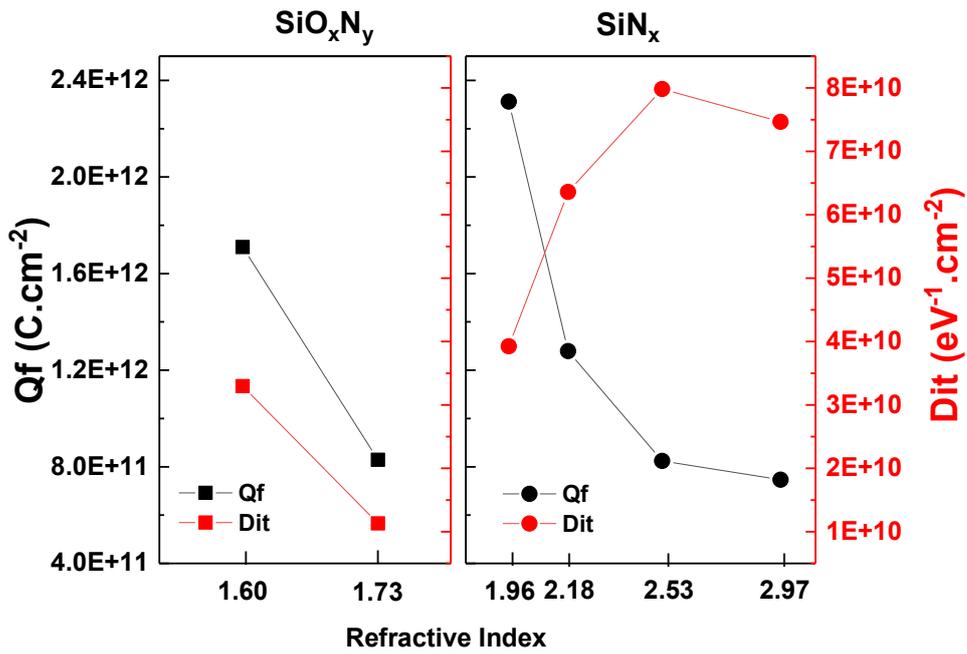
Figure 4.12. Calculated Q_f and D_{it} values of the fabricated dielectric layers with different refractive indices.

4.1.4   PCD Measurements : iV$_{oc}$ Values
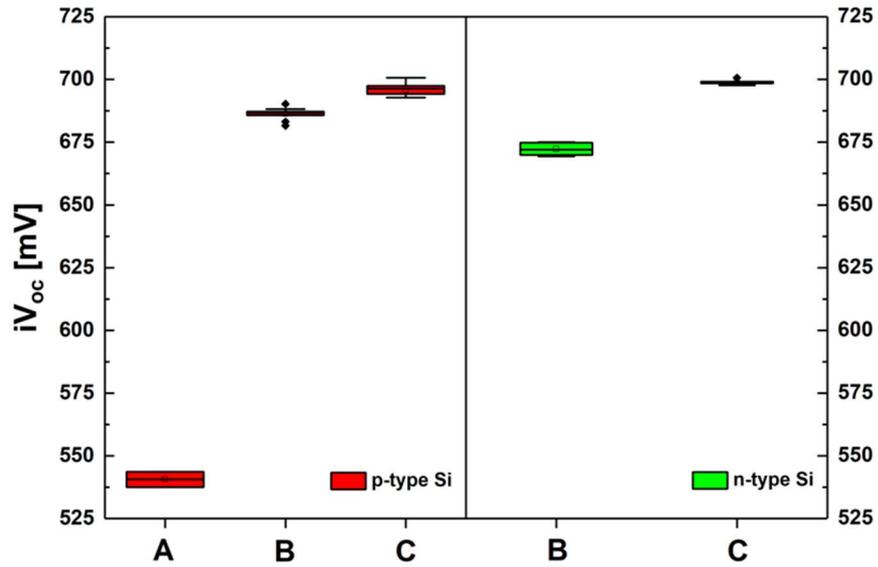
Figure 4.13. iV$_{oc}$ values of the passivation samples on p-type and n-type textured Si wafers after fast firing process.

In *Figure 4.13*, measured iV$_{oc}$ values of the symmetrical passivation samples with no emitter on p-type and n-type textured Si wafers are shown. Films used in passivation are selected for their lowest D$_{it}$ and highest Q$_f$ values. Sample A and B represents films with index of 1.73 and 1.96 respectively. In sample C, few nm of film with index of 1.73 is deposited beneath the SiN$_x$ film with an optical constant of 1.96. Although sample A has lowest D$_{it}$ value, chemical and field-effect passivation is not provided due to its low H density and Q$_f$ value. Sample B has far better iV$_{oc}$ value even its D$_{it}$ is higher than sample A because its Q$_f$ and H density is higher. When few nm of SiO$_x$N$_y$ film with an index of 1.73 is deposited under the SiN$_x$ film with an index of 1.96, iV$_{oc}$ is getting better due to lower D$_{it}$ value, thus lower surface recombination. Same scenario is also true for the samples fabricated with n-type Si wafers. For both wafer types, iV$_{oc}$ values of 700 mV have been reached with thin SiO$_x$N$_y$ film deposited at the Si interface.

4.2 Rear Surface Passivation: Optimization of Capping SiN$_x$ Deposited on 5nm of Al$_2$O$_3$ Layer

Capping layer deposited over 5 nm of Al$_2$O$_3$ layer is investigated by conducting C-V, PCD and EQE measurements. In this manner, two distinct SiN$_x$ stoichiometries with indices 1.96 and 2.53 are deposited on Al$_2$O$_3$ layer after activation process.

4.2.1 C-V Measurement of Al$_2$O$_3$/SiN$_x$ Stack Layers

Figure 4.14 (a) shows the calculated Q$_f$ density of non-fired 95 nm of SiN$_x$ and 5nm of Al$_2$O$_3$ films. Contrary to SiN$_x$ films, 5 nm of Al$_2$O$_3$ film has Q$_f$ with negative polarity. In *Figure 4.14*(b), calculated Q$_f$ of Al$_2$O$_3$/SiN$_x$ stack layers are given. Q$_f$ of the Al$_2$O$_3$/SiN$_x$ stack with index of 1.96 has improved with increasing peak firing temperature; however, Q$_f$ of the Al$_2$O$_3$/2.53 stack has reduced. Thus, this could affect the field-effect passivation quality of the Al$_2$O$_3$/2.53 stack.
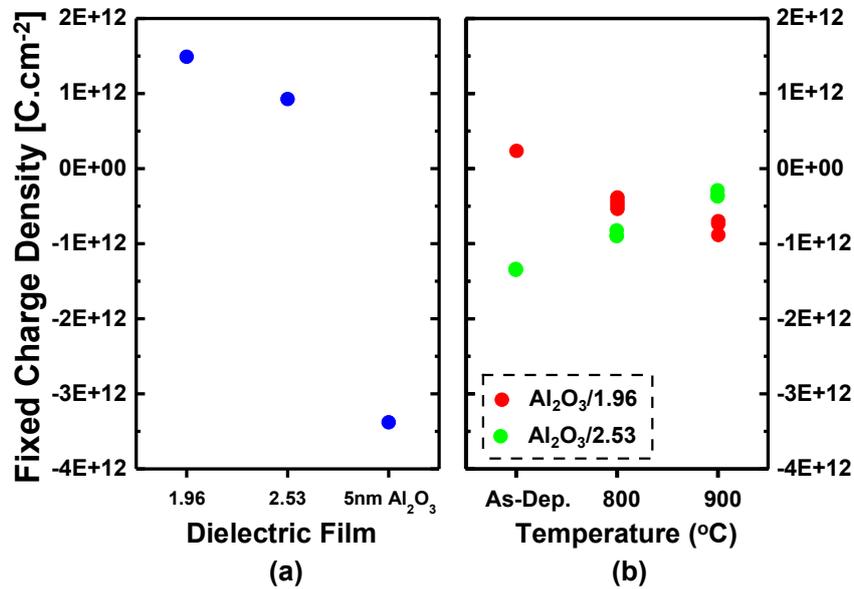
Figure 4.14. Calculated fixed charge densities of (a) unfired SiN$_x$ films with index of 1.96 and 2.53 and 5 nm of Al$_2$O$_3$ layer (left) (b) unfired and fired stack layers of Al$_2$O$_3$/1.96 and Al$_2$O$_3$/2.53.

44

4.2.2 PCD Measurements of Al₂O₃/SiNₓ Stack Layers

Measured iV_{oc} values of the corresponding Al₂O₃/SiNₓ stacks on symmetrical etched samples are given in *Figure 4.15*. iV_{oc} of the Al₂O₃/SiNₓ stack with lower index SiNₓ has suddenly decreased while SiNₓ with lower index resist to higher peak temperatures. This is attributed to the degradation of Si-bulk with excess H released from the SiNₓ film. According to the Lelievre (2009) and Jafari (2019), SiNₓ with higher index releases its H earlier than one with lower index [51],[52]. Although Q_f of the Al₂O₃/SiNₓ with lower refractive index of SiNₓ is improved with higher peak firing temperatures, iV_{oc} values do not show the same trend that Si-bulk degradation by H atoms are more dominant on the passivation performance of the Si wafer.
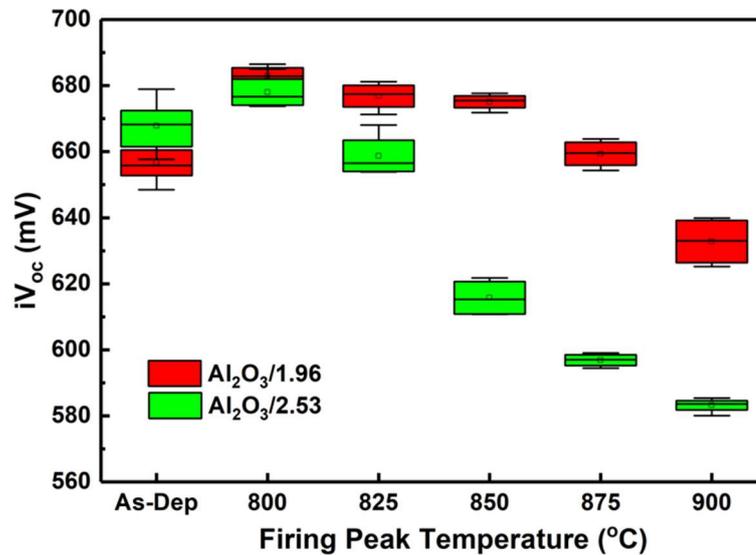
Figure 4.15. iVoc variation of symmetrically Al₂O₃/SiNₓ passivated p-Si wafers with different SiNₓ stoichiometries under various firing peak temperatures.

4.2.3 EQE Measurements of the fabricated PERC Solar Cells that rear surface passivation is held by Al₂O₃/SiNₓ Stack Layers

In *Figure 4.16*, EQE curves of the fabricated PERC solar cells passivated by Al$_2$O$_3$/SiN$_x$ stack layers are given. Since the ARC layers are kept the same for the two cell structures, UV response of both samples are the same. Al$_2$O$_3$/SiN$_x$ stack with lower refractive index of SiN$_x$ has better IR response, thus better surface passivation.
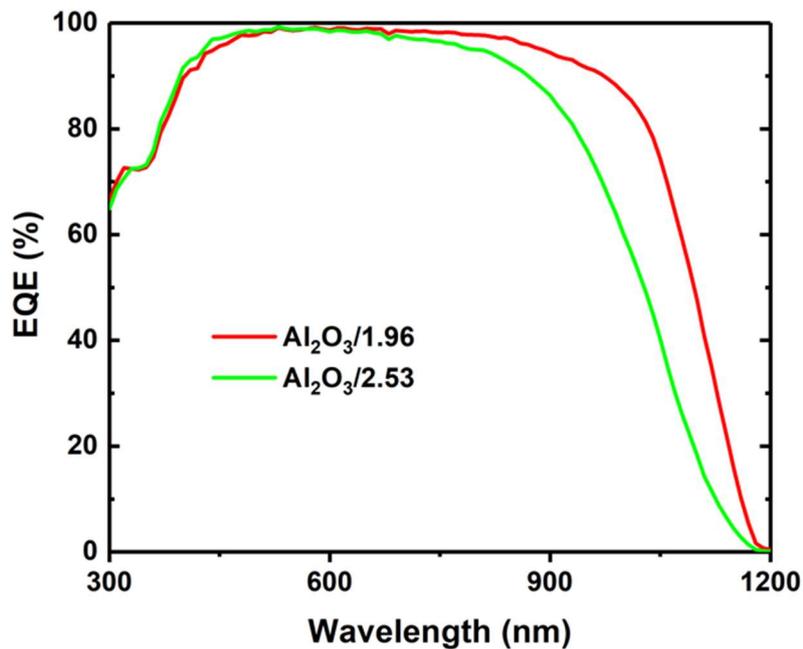
Figure 4.16. EQE curves of the fabricated PERC solar cells passivated by Al$_2$O$_3$/SiN$_x$ stack layers.

4.3 Front Surface Passivation: Optimization of ARC Layer

4.3.1 Simulation of ARC Layer

ARC layer is critical for obtaining highest J_{Gen} value in the Si-bulk with reducing absorption of light in the SiN_x/SiO_xN_y dielectric layers. According to the given optical properties of the fabricated films in section 4.1.1, SiN_x/SiO_xN_y stack layers are simulated for being used as ARC layer with OPAL software [3] while keeping optimum single ARC layer with an index of 1.96 as a reference [53]. As light source the AM 1.5 AG 1 sun spectrum is used, and the surface of the Si is selected as random upright pyramids. In Table 4.3, optical constants of the optimized ARC layers are given with their recipe name. For the SiN_x/SiO_xN_y stack layers, SiO_xN_y with index 1.73 is used due to its zero absorption in the 300-1000 nm of wavelength region.

Table 4.3. *Optical properties of the optimized ARC layers.*

	1st Layer		*2nd Layer*	
Name of the Recipe	*Ref. Index @ 632 nm*	*Thickness (nm)*	*Ref. Index @ 632 nm*	*Thickness (nm)*
new1	1.96	80	-	-
new8	2.18	33	1.73	56
new11	2.53	28	1.73	65
new15	2.04	25	1.73	64

Figure 4.17 shows the simulated reflectance and absorbance curves for the stated ARC recipes in the Table 4.3. While increasing the refractive index of the 1st layer of the ARC layer, reflection is reducing in UV portion of the spectrum significantly. However, absorbance in the film drastically rises for the SiN_x film with higher

refractive indices that these results are well correlated with the *Figure 4.3* where absorption coefficients of the fabricated films were given. Recipe name with new1 which is kept as reference for the optimum single ARC layer shows no absorbance but has the highest reflection among the other recipes.
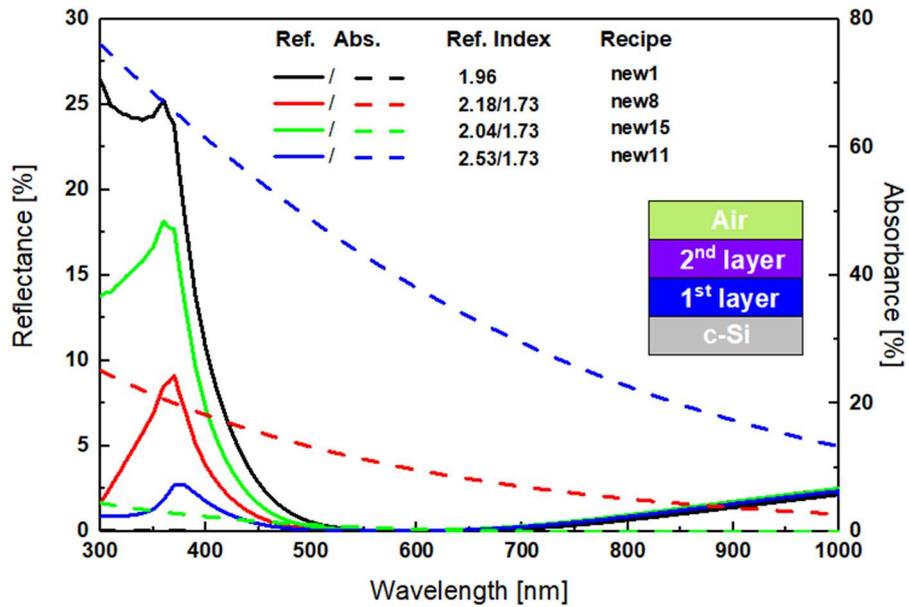
Figure 4.17. Simulated reflectance and absorbance curves of the ARC layers.

The loss mechanisms behind the J_{Gen} value such as absorption in the film and reflection from the surface are detailed in Table 4.4. As increasing refractive index of the 1st layer which is SiN$_x$ film, reflection in UV part is reduced significantly but absorption in the film increases enormously. new15 recipe has the highest J_{Gen} value according to the simulation results.

Table 4.4 *Simulated losses in J_{Gen} due to Reflection from the surface and absorption in the ARC layer.*

Name of the Recipe	Loss Mechanism in J_{Gen} $[mA.cm^{-2}]$		J_{Gen} $[mA.cm^{-2}]$
	Reflection	Absorption	
New1	0.78	0.21	43.45
New8	0.48	0.36	43.60
New11	0.36	1.30	42.78
New15	0.64	0.01	43.79

4.3.2 PCD Measurements of the Front Surface Passivation Samples with Optimum ARC Layers

Symmetrical passivation sample were fabricated to see the performance of ARC layers on the diffused wafers with a sheet resistance of 87 Ω/sq. In *Figure 4.18*, measured iV_{oc} values for non-fired and fired at 800°C set peak firing temperature are given for the ARC layers stated in the previous section. new11 recipe with highest refractive index at the 1st layer has highest iV_{oc} value for non-fired case. This is because deposition temperature is high enough for release of H from the SiN_x layer during the film deposition and reducing the D_{it} values. However, after fast-firing process, new11 recipe has the lowest iV_{oc} values among the others due to excessive H release degraded the Si-bulk. iV_{oc} values of the new1, new8 and new15 are almost the same. Depositing few nm of the SiO_xN_y film with lowest D_{it} value at the Si-SiN_x interface, iV_{oc} value of the fired passivation samples are almost 15 mV higher. This fact shows the importance of lowering D_{it} value at the Si-SiN_x interface for improving the passivation quality. PERC solar cells with int+new15 recipe was not fabricated.
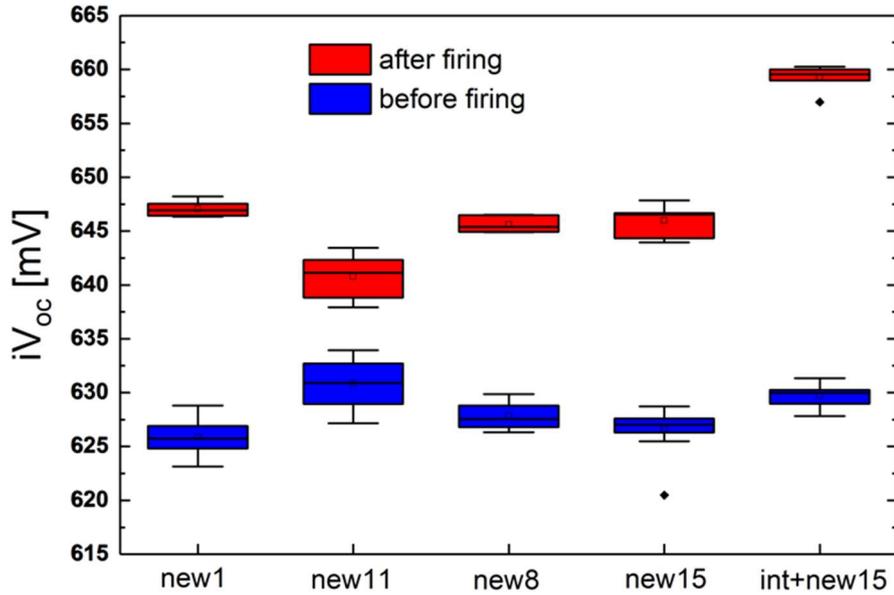
Figure 4.18. iV$_{oc}$ values of the symmetrically diffused samples passivated with with optimized ARC layers.

4.3.3 I-V Results of the Fabricated PERC Solar Cells

I-V results of the fabricated PERC solar cells measure by AAA class flash simulator are given in the *Figure 4.19*. J$_{sc}$ values for new11 recipe are lower than the others, which can be attributed to the more absorption of light by the SiN$_x$ layer. However, J$_{sc}$ increases significantly for the cells with SiN$_x$ having a lower refractive index. Moreover, V$_{oc}$ values are in the same trend as the iV$_{oc}$ results shown in *Figure 4.18*. Gain in J$_{sc}$ values comparing recipes new15 and new8 is well correlated with the performed simulation results on J$_{Gen}$ values given in section 4.3.1 on optimization.
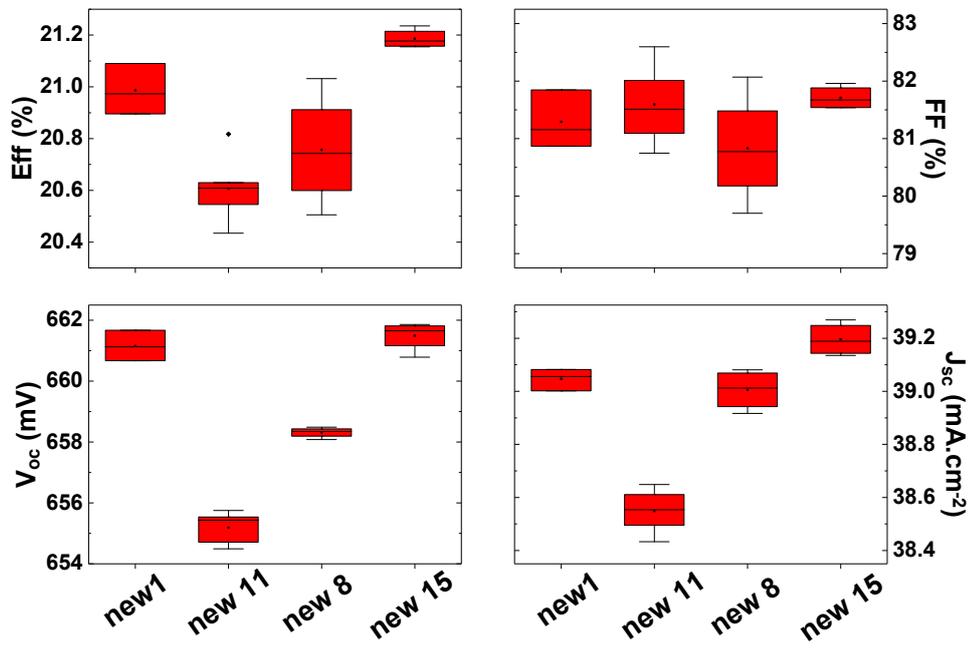
Figure 4.19. I-V results of the fabricated PERC solar cells.

CHAPTER 5

CONCLUSION

In this thesis, fabricated SiN_x and SiO_xN_y films with different stoichiometries were optimized for PERC solar cell. In that manner, stoichiometry of the films was changed by varying process gas flows. Then, optical constants such as refractive index, extinction coefficient and thickness were measured with SE. Increase in refractive index of the films resulted in higher extinction coefficient, thus greater absorption of light by dielectric layer.

H density of the films were calculated by measured IR spectrum in the range of 450-3800 cm^{-1}. For the calculation of H density, Si-H and N-H stretching modes were deconvoluted from the obtained spectrum and maxima of peaks were used in the calculation in terms of absorption coefficient. Films with higher refractive index were rich in H content where SiO_xN_y films were poorer.

Electrical properties of the $Si-SiN_x/SiO_xN_y$ interface were analyzed with fabricated MIS capacitors. Q_f of the films were calculated by using V_{FB} extracted from the C-V graph at 1 MHz of frequency. Q_f of the SiN_x films were increasing for lower indices. Moreover, D_{it} of the films was in the opposite trend with the Q_f. that means SiN_x film with smaller index has lower D_{it}. However, SiO_xN_y film with index of 1.73 has the smallest D_{it} value which is related to the higher Si-O density that is obvious from the deconvoluted FTIR peaks.

Prepared p-type textured Si wafers symmetrically passivated with SiO_xN_y, SiN_x and SiO_xN_y/SiN_x layers were exposed to fast-firing process. Then, iV_{oc} values were compared for different passivation layers. It is seen that SiO_xN_y with lowest D_{it} did not passivate the wafer, but SiN_x layer did. This is mainly due to inadequate field-effect and chemical passivation resulting from low H and Q_f density for the SiO_xN_y film. In addition, thin SiO_xN_y film just beneath the SiN_x film improved the iV_{oc}

because low D_{it} at the interface reduced the surface recombination which is a must for perfect passivation.

Effect of SiN_x stoichiometry on Al_2O_3 layer at rear surface was investigated with performed experiments. Two SiN_x films with different stoichiometries were deposited on Al_2O_3 layer. C-V results revealed that Q_f density of the Al_2O_3/SiN_x stack layer with lower index of SiN_x had improved with peak of the fast-firing process. Also, PCD measurements on symmetrically etched passivation samples showed that Al_2O_3/SiN_x stack with lower index of SiN_x film resisted to relatively higher peak firing temperatures. Since lower refractive index of SiN_x with low H density did not degrade the bulk as the one with higher refractive index. This is because SiN_x with higher refractive index releases its H earlier. The EQE curves in IR region had also proven the fact that SiN_x with lower index deposited on Al_2O_3 layer perfectly passivated the rear surface of the PERC solar cell.

Optimization of ARC layer requires optimum reflection with considerably negligible absorption in dielectric layers and better passivation for emitter region. ARC layers were deposited with combination of two different dielectrics: at the bottom (above Si surface) SiN_x with three different stoichiometries and SiO_xN_y film with index of 1.60 at top of SiN_x layer. When three ARC layers simulated, SiN_x with highest refractive index had smallest reflection but absorption of light by dielectric reached to maximum. SiN_x with smallest refractive index had higher reflection value considering the other two ARC layers but absorption was minimal that resulted in higher J_{Gen} value with absolute 0.19 mA.cm^{-2}. PCD measurement results taken from passivated textured wafers with emitter showed that ARC layer with lower index of SiN_x film had relatively higher iV_{oc} value. This is mainly attributed to higher Q_f and lower D_{it} value for that compositiondeposited on top of Si surface. The I-V results obtained from fabricated PERC solar cells with optimized ARC layers showed the same trend with reflection simulation results.

In the scope of these promising results, PECVD deposited SiO_xN_y film together with SiN_x film has advantage of higher optical band-gap and no or minimal absorbance

which makes it a perfect candidate for fabricating an optimum ARC layer with lower reflection. Besides, incorporation of O atom in its stoichiometry inspires reducing the D_{it} over the Si interface that enables higher iV_{oc}, thus better surface passivation. Also, H supply of SiN_x film is a crucial for passivating D_{it} over the Si surface.

REFERENCES

[1]   K. Kim, S. K. Dhungel, J. Yoo, S. Jung, D. Mangalaraj, and J. Yi, "Hydrogenated silicon-nitride thin films as antireflection and passivation coatings for multicrystalline silicon solar cells," *J. Korean Phys. Soc.*, vol. 51, no. 5, pp. 1659–1662, 2007, doi: 10.3938/jkps.51.1659.

[2]   J. Dupuis *et al.*, "Optical and structural properties of silicon oxynitride deposited by plasma enhanced chemical vapor deposition To cite this version : HAL Id : in2p3-00734027 Optical and structural properties of silicon oxynitride deposited by Plasma Enhanced Chemical Vap," 2019.

[3]   K. R. Mcintosh and S. C. Baker-finch, "OPAL 2 : Rapid Optical Simulation of Silicon Solar Cells OPAL 2 : Rapid Optical Simulation of Silicon Solar Cells," no. June 2012, 2015, doi: 10.1109/PVSC.2012.6317616.

[4]   A. Einstein, "On a Heuristic Point of View Concerning the Production and Transformation of Light," *Ann. der Phys. 17*, pp. 132–148, 1905.

[5]   J. Seiffe *et al.*, "Surface passivation of crystalline silicon by plasma-enhanced chemical vapor deposition double layers of silicon-rich silicon oxynitride and silicon nitride," *J. Appl. Phys.*, vol. 109, no. 3, 2011, doi: 10.1063/1.3544421.

[6]   C. Sun, F. E. Rougieux, and D. Macdonald, "defects in crystalline silicon A unified approach to modelling the charge state of monatomic hydrogen and other defects in crystalline silicon," vol. 045702, 2015, doi: 10.1063/1.4906465.

[7]   S. Joonwichien, S. Simayi, K. Shirasawa, K. Tanahashi, and H. Takato, "Thermal Treatment Effects on Flat-band Voltage Shift in Atomic-layer-deposited Alumina or Aluminum Oxide/Silicon Nitride Passivation Stacks," *Energy Procedia*, vol. 92, pp. 353–358, 2016, doi: 10.1016/j.egypro.2016.07.112.

[8] V. Sharma, "Study of Charges Present in Silicon Nitride Thin Films and Their Effect on Silicon Solar Cell Efficiencies," 2013.

[9] S. Jafari, Chaitanya, J. Dwan, J. Hirsch, N. Bernhard, and D. Lausch, "COMPOSITION-DEPENDENT HYDROGEN EFFUSION AND DIFFUSION MECHANISM WITHIN a-SiN$_x$:H," 2018.

[10] D. Hinken *et al.*, "Determination of the base-dopant concentration of large-area crystalline silicon solar cells," *IEEE Trans. Electron Devices*, vol. 57, no. 11, pp. 2831–2837, 2010, doi: 10.1109/TED.2010.2064777.

[11] V. Verlaan, C. H. M. Van Der Werf, W. M. Arnoldbik, H. D. Goldbach, and R. E. I. Schropp, "Unambiguous determination of Fourier-transform infrared spectroscopy proportionality factors: The case of silicon nitride," *Phys. Rev. B - Condens. Matter Mater. Phys.*, vol. 73, no. 19, 2006, doi: 10.1103/PhysRevB.73.195333.

[12] E.Bustarret, M.Bensouda, M.C.Habrard, J.C.Bruyere, S.Poulin, and S.C.Gujrathi, "Configurational statistics in a-SiN$_x$:H alloys: A quantitative bonding analysis," *Phys. Rev. B - Condens. Matter Mater. Phys.*, vol. 38, no. 12, pp. 8171–8184, 1988.

[13] B. J. Hallam *et al.*, "Hydrogen passivation of B-O defects in Czochralski silicon," *Energy Procedia*, vol. 38, no. Lid, pp. 561–570, 2013, doi: 10.1016/j.egypro.2013.07.317.

[14] F. Giorgis *et al.*, "Optical, structural and electrical properties of device-quality hydrogenated amorphous silicon-nitrogen films deposited by plasma-enhanced chemical vapour deposition," *Philos. Mag. B Phys. Condens. Matter; Stat. Mech. Electron. Opt. Magn. Prop.*, vol. 77, no. 4, pp. 925–944, 1998, doi: 10.1080/13642819808206395.

[15] F. Demichelis, F. Giorgis, and C. F. Pirri, "Compositional and structural analysis of hydrogenated amorphous silicon—nitrogen alloys prepared by plasma-enhanced chemical vapour deposition," *Philos. Mag. B Phys.*

Condens. Matter; Stat. Mech. Electron. Opt. Magn. Prop., vol. 74, no. 2, pp. 155–168, 1996, doi: 10.1080/01418639608240333.

[16] I. Jonak-Auer, R. Meisels, and F. Kuchar, "Determination of the hydrogen concentration of silicon nitride layers by Fourier transform infrared spectroscopy," *Infrared Phys. Technol.*, vol. 38, no. 4, pp. 223–226, 1997, doi: 10.1016/S1350-4495(97)00011-X.

[17] W. A. Lanford and M. J. Rand, "The hydrogen content of plasma-deposited silicon nitride," *J. Appl. Phys.*, vol. 49, no. 4, pp. 2473–2477, 1978, doi: 10.1063/1.325095.

[18] F. Ay and A. Aydinli, "Comparative investigation of hydrogen bonding in silicon based PECVD grown dielectrics for optical waveguides," vol. 26, pp. 33–46, 2004, doi: 10.1016/j.optmat.2003.12.004.

[19] W. L. Warren and J. Electrochem, "Paramagnetic Point Defects in Amorphous Silicon Dioxide and Amorphous Silicon Nitride Thin Films : II . Paramagnetic Point Defects in Amorphous Silicon Dioxide and Amorphous Silicon Nitride Thin Films," 1992.

[20] J. R. Elmiger and M. Kunst, "Investigation of the silicon-plasma silicon nitride interface with in situ transient photoconductivity measurements," *Appl. Surf. Sci.*, vol. 103, no. 1, pp. 11–18, 1996, doi: 10.1016/0169-4332(96)00471-0.

[21] L. E. Black and W. M. M. (Erwin. Kessels, "Investigation of crystalline silicon surface passivation by positively charged PO_x/Al_2O_3 stacks," *Sol. Energy Mater. Sol. Cells*, vol. 185, no. 2018, pp. 385–391, 2018, doi: 10.1016/j.solmat.2018.05.007.

[22] J. F. Lelièvre, E. Fourmond, A. Kaminski, O. Palais, D. Ballutaud, and M. Lemiti, "Study of the composition of hydrogenated silicon nitride SiN_x:H for efficient surface and bulk passivation of silicon," *Sol. Energy Mater. Sol. Cells*, vol. 93, no. 8, pp. 1281–1289, 2009, doi: 10.1016/j.solmat.2009.01.023.

[23]   V. Sharma, C. Tracy, D. Schroder, M. Flores, B. Dauksher, and S. Bowden, "Study and manipulation of charges present in silicon nitride films," *Conf. Rec. IEEE Photovolt. Spec. Conf.*, pp. 1288–1293, 2013, doi: 10.1109/PVSC.2013.6744377.

[24]   A. Muntahi and S. Ahmed, "Chapter 1 MOSCap Tool on nanoHUB.org : A Primer," 2012.

[25]   D. K. Schroder, *SEMICONDUCTOR MATERIAL AND DEVICE CHARACTERIZATION*, 3rd ed. Wiley-Interscience, 2006.

[26]   A. Tatarog, "Analysis of surface states and series resistance in Au / n-Si Schottky diodes with insulator layer using current – voltage and admittance – voltage characteristics," vol. 84, pp. 363–368, 2010, doi: 10.1016/j.vacuum.2009.07.003.

[27]   A. Singh and D. Fisica, "Solid-Slate EIectronics Vol. 33, No. I, pp. 11-19, 1990," vol. 33, no. I, pp. 11–19, 1990.

[28]   M. G. Guvench, "Automated measurement of MOS capacitance and determination of MOS process parameters in the microfabrication laboratory," *ASEE Annu. Conf. Proc.*, 1997, doi: 10.18260/1-2--6431.

[29]   C. N. Berglund, "Surface States at Steam-Grown Silicon-Silicon Dioxide Interfaces," *IEEE Trans. Electron Devices*, vol. 13, no. 10, 1966.

[30]   N. Novkovski, "Determination of interface states in metal(Ag,TiN,W)-Hf:Ta$_2$O$_5$/SiO$_x$N$_y$-Si structures by different compact methods," *Mater. Sci. Semicond. Process.*, vol. 39, pp. 308–317, 2015, doi: 10.1016/j.mssp.2015.05.028.

[31]   S. Joonwichien, S. Simayi, K. Shirasawa, and K. Tanahashi, "Thermal treatment effects on flat-band voltage shift in atomic-layer- deposited alumina or aluminum oxide / silicon nitride passivation stacks," *Energy Procedia*, vol. 92, pp. 353–358, 2016, doi: 10.1016/j.egypro.2016.07.112.

[32] R. A. Sinton, A. Cuevas, and R. A. Sinton, "Contactless determination of current – voltage characteristics and minority-carrier lifetimes in semiconductors from quasi-steady-state photoconductance data Contactless determination of current – voltage characteristics and minority- carrier lifetimes in," vol. 2510, no. 1996, pp. 1–4, 2015, doi: 10.1063/1.117723.

[33] G. E. Jellison, F. A. Modine, P. Doshi, and A. Rohatgi, "Spectroscopic ellipsometry characterization of thin-film silicon nitride," pp. 193–197, 1998.

[34] Y. Wan, K. R. McIntosh, and A. F. Thomson, "Characterisation and optimisation of PECVD SiN$_x$ as an antireflection coating and passivation layer for silicon solar cells," *AIP Adv.*, vol. 3, no. 3, pp. 0–14, 2013, doi: 10.1063/1.4795108.

[35] G. Tan, M. F. Lemon, and R. H. French, "Optical Properties and London Dispersion Forces of Amorphous Silica Determined by Vacuum Ultraviolet Spectroscopy and Spectroscopic Ellipsometry," vol. 92, pp. 1885–1892, 2003.

[36] H. Charifi, A. Slaoui, J. P. Stoquert, H. Chaib, and A. Hannour, "Opto-Structural Properties of Silicon Nitride Thin Films Deposited by ECR-PECVD," no. February, pp. 7–16, 2016.

[37] T. Grigaitis, A. Naujokaitis, S. Tumėnas, G. Juška, and K. Arlauskas, "Characterization of silicon nitride layers deposited in three-electrode plasma-enhanced CVD chamber CHARACTERIZATION OF SILICON NITRIDE LAYERS DEPOSITED IN THREE-ELECTRODE PLASMA-ENHANCED CVD CHAMBER," no. May, 2015, doi: 10.3952/physics.v55i1.3056.

[38] G. N. Parsons and G. Lucovsky, "Silicon-hydrogen bond-stretching vibrations in hydrogenated amorphous silicon-nitrogen alloys," *Phys. Rev. B - Condens. Matter Mater. Phys.*, vol. 41, no. 3, 1990.

[39] B. F. Hanyaloglu and E. S. Aydil, "Low temperature plasma deposition of silicon nitride from silane and nitrogen plasmas," *J. Vac. Sci. Technol. A Vacuum, Surfaces, Film.*, vol. 16, no. 5, pp. 2794–2803, 1998, doi:

10.1116/1.581424.

[40] M. Boulesbaa, "Optical and physicochemical properties of hydrogenated silicon nitride thin films : Effect of the thermal annealing," *Spectrosc. Lett.*, vol. 50, no. 1, pp. 5–12, 2017, doi: 10.1080/00387010.2016.1262425.

[41] W.-Y. Ding *et al.*, "Deposition of Hydrogen-Free Silicon Nitride Thin Films by Microwave ECR plasma Enhanced Magnetron Sputtering at Room Temperature," *chinese Phys. Lett.*, vol. 22, no. 9, p. 2332, 2005.

[42] D. Bredemeier, D. Walter, R. Heller, and J. Schmidt, "Impact of Silicon Nitride Film Properties on Hydrogen in-Diffusion Into Crystalline Silicon," *36th Eur. Photovolt. Sol. Energy Conf. Exhib.*, no. November, pp. 112–115, 2019.

[43] P. Wang, S. Jin, T. Lu, C. Cui, D. Yang, and X. Yu, "Negatively charged silicon nitride films for improved p-type silicon surface passivation by low-temperature rapid thermal annealing," *J. Phys. D. Appl. Phys.*, vol. 52, no. 34, 2019, doi: 10.1088/1361-6463/ab2ab9.

[44] S. Helland, "Electrical Characterization of Amorphous Silicon Nitride Passivation Layers for Crystalline Silicon Solar Cells," 2011.

[45] E. H. Nicollian and A. Goetzberg, "The Si-SiO$_2$ Interface - Electrical Properties as Determined by the Metal-Insulator_Silicon Conductance Technique," *Bell Syst. Tech. J.*, vol. 46, no. 6, pp. 1055–1133, 1967.

[46] M. Theodoropoulou *et al.*, "Interface traps density of anodic porous alumina films of different thicknesses on Si," *J. Phys. Conf. Ser.*, vol. 10, no. 1, pp. 222–225, 2005, doi: 10.1088/1742-6596/10/1/055.

[47] D. K. Basa, M. Bose, and D. N. Bose, "Capacitance–voltage measurements on plasma enhanced chemical vapor deposited silicon nitride films," *J. Appl. Phys.*, vol. 87, no. 9, pp. 4324–4326, 2000, doi: 10.1063/1.373073.

[48] J. Robertson and M. J. Powell, "Gap states in silicon nitride," *Appl. Phys.*

Lett., vol. 44, no. 4, pp. 415–417, 1984, doi: 10.1063/1.94794.

[49]   H. Yang, E. Wang, H. Wang, and W. Guo, "Industrail technology of passivated emitter and rear cells with silicon oxynitride and silicon nitride as rear passivation for high efficiency BIPV modules," *Energy Procedia*, vol. 88, pp. 389–393, 2016, doi: 10.1016/j.egypro.2016.06.007.

[50]   J. Dupuis, E. Fourmond, J. F. Lelièvre, D. Ballutaud, and M. Lemiti, "Impact of PECVD SiON stoichiometry and post-annealing on the silicon surface passivation," vol. 516, pp. 6954–6958, 2008, doi: 10.1016/j.tsf.2007.12.026.

[51]   J. F. Lelièvre *et al.*, "Efficient silicon nitride SiN_x:H antireflective and passivation layers deposited by atmospheric pressure PECVD for silicon solar cells," *Prog. Photovoltaics Res. Appl.*, vol. 27, no. 11, pp. 1007–1019, 2019, doi: 10.1002/pip.3141.

[52]   S. Jafari, J. Hirsch, D. Lausch, M. John, and S. Meyer, "Composition limited hydrogen effusion rate of a-SiN_x : H passivation stack Composition Limited Hydrogen Effusion Rate of a-SiN_x : H Passivation Stack," vol. 050004, no. August, 2019.

[53]   J. Kim, "Optimization of SiN_x layer for solar cell using computational method," *Curr. Appl. Phys.*, vol. 11, no. 1, pp. S39–S42, 2011, doi: 10.1016/j.cap.2010.11.048.